UNIVERSITY OF CRETE
SCHOOL OF SCIENCES & ENGINEERING
DEPARTMENT OF MATERIALS SCIENCE AND TECHNOLOGY

Development and Characterization of $Ni_2P/CuCo_2S_4$ Composite Nanostructures for Electrocatalytic Overall Water Splitting

Master Thesis

Sofia Bra

Supervisor: Prof. Gerasimos Armatas

Heraklion 2022

Preface

This M.Sc. thesis was conducted in the department of Materials Science and Technology at the University of Crete (UOC) in Heraklion under the supervision and guidance of Professor Gerasimos S. Armatas, in the academic years 2020-22. The materials used in this dissertation were fabricated at Laboratory of Advanced Materials Chemistry, Department of Materials Science and Technology at the University of Crete. The X-ray diffraction (XRD), energy-dispersive X-ray spectroscopy (EDS), X-ray photoelectron spectroscopy (XPS) and transmission electron microscopy (TEM) measurements were carried out using the facilities of the School of Sciences and Engineering of the University of Crete. The Ultraviolet-visible spectroscopy measurements were performed at the Institute of Electronic Structure and Laser, Foundation for Research & Technology (IESL-FORTH).

Acknowledgments

My first and foremost sense of gratitude goes to Prof. Gerasimos Armatas, for having given me the wonderful opportunity to be a part of his laboratory group since September 2019 and perform my Bachelor's and Master's graduation research projects here. I would also like to thank Associate Professor Constantinos Stoumpos and Associate Professor George Kopidakis of the Department of Materials Science and Technology for performing the DFT calculations (Prof. G. Kopidakis) and agreeing to be my external committee members. Having thanked my professors, I now take this opportunity to thank my daily supervisor, Dr. Ioannis Vamvasakis, for EIS and EDS training. Thank you very much for being a very patient and supportive guide over this period. Your easy-to-approach attitude made things easier for me to interact with you anytime, it was my pleasure to work with you. Also, I would like to thank PhD student, Evangelos K. Andreou, for providing me the training and the assistance to complete the materials' characterizations such as XPS and XRD. It was my pleasure working with you too, and I wish you lots of success in completing your PhD. My sincerest gratitude goes to all the members of our group for their direct or indirect contributions to my thesis. Last but not least, I would like to thank my parents and my friends, who have been an epitome of love and support for me over the last two years. Thank you!

Sofia Bra

Abstract

The development of highly effective, stable and inexpensive catalysts is an important target in the research of water electrolysis and hydrogen production. A key pursuit of current research efforts is to increase the exposure and accessibility of the catalyst's active sites as well as to improve the kinetics of the reaction. This is achievable by combining suitable chemical components in the same material, which could induce electronic band structure modulation and efficient charge-transfer dynamics, with a properly designed nanostructured morphology, which offers a rich density of active sites and large interfacial contact area. The purpose of this master's thesis is to fabricate and characterize new nanostructured heterostructures of Ni_2P and $CuCo_2S_4$ composition and to investigate the electrocatalytic activity of these materials towards the electrochemical water splitting and hydrogen evolution reaction (HER). The morphology, composition and crystal structure of the $Ni_2P/CuCo_2S_4$ composite catalysts were characterized by a combination of electron microscopy, EDS microprobe analysis, X-ray photoelectron spectroscopy (XPS) and X-ray diffraction techniques. These results indicated that $Ni_2P/CuCo_2S_4$ heterostructures adopt a cubic thiospinel structure and a hexagonal Ni_2P phase (in 10-15 nm size), while their surface is endowed with various loadings of nickel phosphide, i.e., 15, 20, 30 and 40 wt.%. Experimental optical absorption, valence band XPS and electrochemical spectroscopy studies coupled with theoretical DFT calculations indicated that p-n $Ni_2P/CuCo_2S_4$ junctions provide an increased number of electrochemically active surface sites and an efficient interfacial electronic transport with lower resistance, resulting in a remarkable enhancement in the electrocatalytic H_2 evolution performance. The unmodified $CuCo_2S_4$ sample showed moderate to low electrocatalytic behavior for the hydrogen evolution reaction, giving an overpotential of 348 mV at a current density of 10 $mA \cdot cm^{-2}$ in an alkaline electrolyte (1M KOH). We show that Ni_2P-modification of the $CuCo_2S_4$ surface markedly increases the electrochemical activity by improving the transport efficiency of electrons at the $Ni_2P/CuCo_2S_4$ interface. Thus, the optimized $Ni_2P/CuCo_2S_4$ catalyst at 30 wt.% Ni_2P content reached the lowest overpotential of 183 mV at 10 $mA \cdot cm^{-2}$ current density under alkaline conditions, which is associated with a 78 $mV \cdot dec^{-1}$ Tafel slope, indicating a Volmer-Heyrovsky type mechanism. Chronopotensiometric studies revealed that $Ni_2P/CuCo_2S_4$ is quite stable during the reaction, operating stably for 30 h under a current density of 10 $mV \cdot cm^{-2}$. In addition, the 30% Ni_2P-loaded catalyst showed a very good oxygen evolution reaction (OER) activity with an overpotential of 360 mV at 40 $mA \cdot cm^{-2}$ current density in 1 M KOH electrolyte. When 30% $Ni_2P/CuCo_2S_4$ is used as both anode and cathode in a two-electrode electrochemical cell, it requires only a 1.78 V potential for overall water electrolysis under 10 $mA \cdot cm^{-2}$ current density. Overall, these Ni_2P-modified $CuCo_2S_4$ catalysts demonstrate great potential for renewable hydrogen production technologies, including water electrolysis.

Table of Contents

1. Introduction

1.1 Thiospinels in a nutshell

Spinel compounds, which have a formula of A_3X_4, AB_2X_4, $ABCX_4$ or ABC_3X_8 – with the A, B, C cations occupying some or all of the octahedral and tetrahedral sites in the lattice and X anions (like oxygen and sulfur) arranged in a cubic close-packed structure – exhibit a wide range of unique and appealing characteristics, especially when the elements A, B, C, and X are combined in different ways.[1–4] Thiospinels or sulfur-based spinels (with the X-element in the chemical formula corresponding to sulfur) are the most well-known kind of spinel material with binary, ternary or quaternary composition (Figure 1).[5] The vast majority of thiospinel materials have a $Fd\bar{3}m$ crystalline symmetry, where A-atoms typically occupy the tetrahedral sites, the remaining cation atoms occupy the octahedral sites and the sulfur atoms being tightly packed.[1,2,4,6,7] Due to the thiospinel materials' unique physical and chemical attributes, several research groups have worked hard for more than half a century to understand their properties. Among many interesting traits, thiospinel materials are endowed with remarkable electromagnetic and electrical properties. While certain thiospinels are good magnetic semiconductors and others exhibit metallic behavior, it has been recently demonstrated that the majority of thiospinels have an anti-ferromagnetic ground state.[8,9] Moreover, by being a hot research subject for the last three decades, more interesting findings have been discovered including their photosensitivity and transparency to high-energy photons[10,11] as well as their anisotropic pressure-dependent function, which may find use in defect engineering.[12]

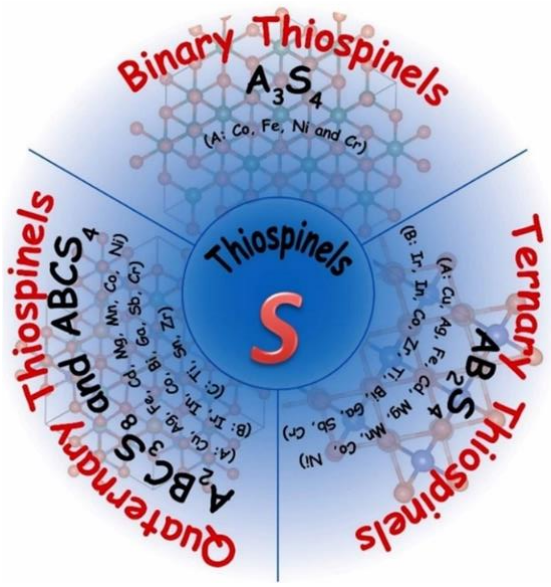

Figure 1: Types of sulfur-based spinel compounds.[5]

1.1.1 The properties of thiospinels

It is anticipated from researchers to discover and develop functional materials of abundant elements, that are also non-toxic and non-hazardous to humans and the environment. In this context, it is possible to create suitable thiospinel materials by taking into consideration the specific characteristics of the environment in which they will be employed. These materials can provide some key characteristics that enable a wide range of applications. For example, Cu- and Cu-Sn based thiospinels have been used as thermoelectric materials, which convert heat energy straight into electrical energy.[13,14] Other Fe-, Co-, Cr-, and Ni-based thiospinels have been shown to exhibit some ferrimagnetism and, as a result, can be used in the fields of information technology. Also, as a metallic and paramagnetic compound, $CuCo_2S_4$ possess interesting magnetic and electronic features under ambient conditions and shows weak anti-ferromagnetism at low temperatures.[15,16] On the other hand, some thiospinel materials have attractive optical properties such as strong photosensitivity and nonlinear optical susceptibility[17,18], and thus, have received a lot of interest for optoelectronic device applications. For instance, $CdIn_2S_4$ nanostructures have the potential to be used in light-emitting diodes (LEDs), as well as photoelectrical and photocatalytic applications.[19–22] Because of the increasing energy demands, these materials have also received significant interest in electrical applications such as electrode materials[23], lithium-ion batteries[24] and supercapacitors[25]. Moreover, due to their diverse compositions and morphologies, thiospinel-based materials have also been utilized in several catalytic reaction.[26–29] Thus, from the utilization perspective of thiospinels, it has been indicated that the variable compositions and characteristics of these materials play a key role for specific applications. Specifically for energy-related applications, some prominent qualities of thiospinels will be discussed in the following section.

1.1.2 Applications in energy

Due to the increasing population, rapid development and ever-increasing use of numerous electronic gadgets, the next decades are projected to see a significant increase in energy demand. To this end, alternative and sustainable energy sources are strongly taken into consideration as a replacement for nonrenewable fossil fuels in order to satisfy the expectations. As mentioned before, due to the appropriateness for various energy storage and conversion applications, such as batteries, super-capacitors, solar cells and catalysts for electrochemical green-fuel production, transition metal sulfides (TMSs), and especially

thiospinels, have recently gained a lot of attention. Figure 2 provides a concise schematic representation of the general range of use of thiospinels in energy-related technologies. Among various types as well as compared to their oxide counterparts, the ternary-structured thiospinels (type AB_2S_4) exhibit favorable properties including better electrical conductivity, superior solar-to-electric conversion efficiency and improved stability. Therefore, in many technological fields, starting from catalysis to energy storage and generation use, ternary thiospinels are leading materials with numerous essential characteristics. [5]

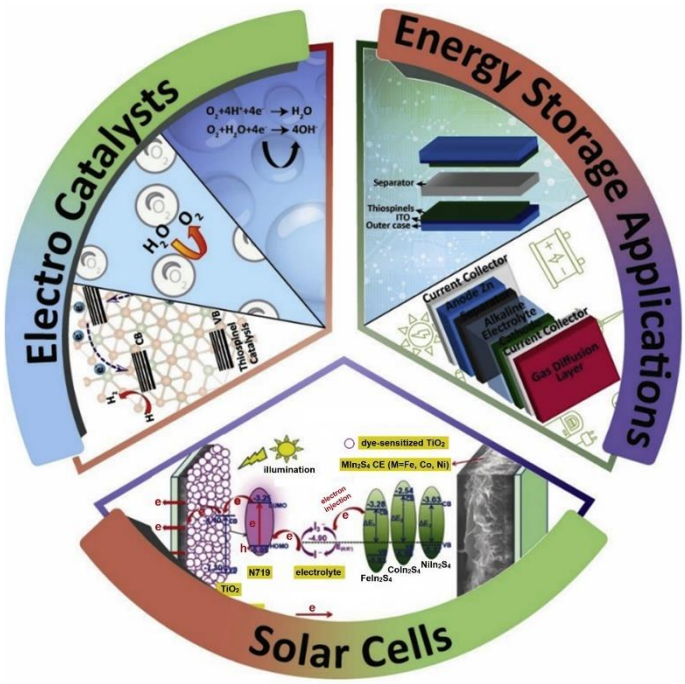

Figure 2: Schematic representation of the various energy applications of thiospinels. [5]

1.1.2.1 Thiospinels as electrocatalysts for hydrogen evolution

In the pursue of green and renewable energy sources to replace the environmentally unfriendly fossil fuels, molecular hydrogen (H_2) plays a crucial role and has been of focus in materials science and chemical engineering in last years.[30,31] In this regard, electrochemical water splitting for the production of H_2 via the hydrogen evolution reaction (HER) has been regarded as a promising process for energy and environmental sustainability. In principle, HER relies on the reduction of water molecules on the surface of a proper electrocatalyst (used as the cathode electrode) to produce hydrogen, according to the following general equation:

$$2H_2O + 2e^- \rightarrow H_2 + 2OH^- \quad (1.1)$$

The efficiency of this reaction mainly depends on the applied electrode potential and the catalytic activity of the electrode material. One of the major challenges is to develop active electrocatalysts that can achieve maximum efficiency (i.e., hydrogen evolution) at the lowest possible overpotential for a specific current density (usually 10 mA cm^{-2}); the basic electrocatalytic principles and reaction mechanisms are described in more detail in section 1.3.

Due to their excellent electrocatalytic activity, several ternary thiospinel catalysts based on nickel, cobalt, copper, iron, and molybdenum divalent and trivalent metal cations have been efficiently used in HER.[32] A recent study by Singh et al.[33], comparing rhodium sulfide ($Rh_{17}S_{15}$) and Rh-based thiospinels ($NiRh_2S_4$, $CoRh_2S_4$, $FeRh_2S_4$, and $CuRh_2S_4$) as HER catalysts in acid electrolytes, showed that the HER activity of thiospinels was lower than that of pure $Rh_{17}S_{15}$. Nevertheless, the highest catalytic activity among all studied thiospinels was found in $NiRh_2S_4$ due to its metallic conductivity, while the most unstable in acidic conditions was $CuRh_2S_4$. In addition, the poor activities of $FeRh_2S_4$ and $CoRh_2S_4$ were attributed to their semiconducting characteristics, making them less favorable for electrocatalytic reactions. In contrast to Rh-based thiospinels, Gervas et al.[34] have studied the correlation of Ni- and Co-enriched ternary thiospinels in energy generation and storage applications. Based on their findings, the Ni-rich thiospinel catalyst showed an improved efficiency as compared with the Co-rich counterpart, exhibiting lower overpotential and enhanced kinetics for the HER under the same conditions. When compared with previous investigations on nickel-cobalt thiospinels[35,36], these results show a clear improvement in electrocatalytic HER. Notably, the above examples indicate that the composition, electronic and conductivity properties are only few characteristics that affect the catalytic activity of thiospinels for the HER and that more work and effort is required in this direction. Table 1, summarizes the electrochemical parameters for some of the most common thiospinel materials used for the hydrogen evolution reaction.

1.1.2.2 Thiospinels as electrocatalysts for oxygen evolution reaction

Besides the HER, the other key half reaction of water electrolysis is the oxygen evolution reaction (OER), as described by the following equation:

$$2H_2O \rightarrow O_2 + 4H^+ + 4e^- \quad (1.2)$$

Briefly, as shown in the reaction equation (1.2), this process involves a four proton-coupled electron transfer and thus becomes thermodynamically and kinetically more complicated and challenging than the two-electron process of the HER. Again, the reaction efficiency relies largely on the applied electrode potential, and the reaction mechanism depends on the electrocatalyst composition and different surface-active sites. Generally, the surface metal cations (M) are considered as the OER active sites where the reaction progresses through a series of surface metal-stabilized intermediates, including the formation of M–O, M–OH and M–OOH species.[32]

A recent work by Wu et al. compared the OER activity of Ni, Cu, Co-based thiospinels ($NiCu_2S_4$ and $CuCo_2S_4$) with that of the corresponding oxide counterparts.[37] The comparative electrochemical results revealed that the examined thiospinels catalyze the OER at a lower current density and at a faster rate than the respective oxides, because of two main reasons: (i) excellent electronic conductivity together with different electronic structures and oxidation states of metals and (ii) higher density of catalytically active sites on the surface of the thiospinel nanostructures. Another complementary study by Wan et al. examined the OER performance of a Ni^{3+}-enriched binary thiospinel Ni_3S_4 porous material.[38] The high valence Ni^{3+} ions together with the hierarchical porous architecture resulted in an advanced OER activity with a rather low overpotential of 257 mV at 10 mA cm^{-2}, and excellent long-term stability of 300 h at 50 mA cm^{-2} for their Ni_3S_4 catalyst. The researchers suggested that the hierarchical porosity increased the number of exposed active sites, promoting mass transport, while the presence of Ni^{3+} ions enhanced the chemisorption of OH^-, which facilitated the electron transfer to the electrode surface during OER. Other publications by Wiltrout et al.[39] and Chauhan et al.[40] have examined the application of $CuCo_2S_4$ thiospinels, synthesized by different methods, as OER electrocatalysts. Chauhan et al. used a hydrothermal synthesis method to produce a hierarchical $CuCo_2S_4$ nanosheet structure, while Wiltrout et al. preferred a solution synthesis method at 200 ^oC to prepare colloidal $CuCo_2S_4$ nanoparticles. The comparative results from the two studies evidenced that the nanosheet structure outperformed the $CuCo_2S_4$ nanoparticles, showing both lower overpotential (310 mV vs. 395 mV at 10 mA cm^{-2}) and better cycling stability. Hence, these findings explicitly demonstrate that for catalysts with the same chemical composition, the catalytic performance can be improved by designing catalyst with specific shape and morphology. Table 1, summarizes the electrochemical parameters of some active thiospinels for the oxygen evolution reaction.

Table 1. Important electrochemical parameters of some common thiospinels for HER and OER.

Catalytic reaction	Thiospinel	Current density	Overpotential
HER	Co_3S_4 [41]	10 mA cm^{-2}	218 mV
	$CoNi_2S_4$ [42]	10 mA cm^{-2}	255 mV
	Fe_3S_4 [43]	10 mA cm^{-2}	185 mV
	$CuCo_2S_4$ [44]	10 mA cm^{-2}	135 mV
	$NiCo_2S_4$ [35]	100 mA cm^{-2}	305 mV
OER	$NiCuCoS_4$ [37]	10 mA cm^{-2}	340 mV
	$CuCo_2S_4$ [39]	10 mA cm^{-2}	395 mV
	Co_3S_4 [41]	10 mA cm^{-2}	283 mV
	Ni_3S_4 [38]	50 mA cm^{-2}	300 mV
	Fe_3S_4 [45]	10 mA cm^{-2}	385 mV

Overall, although many thiospinels are successfully implemented as electrocatalysts for HER and OER applications, still the best performing catalysts in these fields are the precious and expensive Pt/Ir-based materials. Therefore, it is of utmost importance to synthesize new catalysts with high performance and low cost, like thiospinels. In addition, doping the structure with heteroatoms and the combination with appropriate co-catalysts are considered as highly promising strategies to enhance the electrocatalytic performance of single-component catalysts.

1.1.3 The thiospinel $CuCo_2S_4$ and its applications

$CuCo_2S_4$ is a ternary thiospinel material that has been investigated by many researchers in recent years due to the interesting catalytic and optical properties.[39,40,46,47] The crystal structure of this material, like most of the thiospinels, is a spinel cubic structure, see Figure 3. In $CuCo_2S_4$, Cu and Co occupy tetrahedral and octahedral sites, respectively, and its X-ray diffraction (XRD) pattern is very close to that of Co_3S_4 because the two materials have very similar crystal lattices with a lattice constant α of ~9.48 Å. Previous studies have shown interesting optical properties for the $CuCo_2S_4$ thiospinel, exhibiting a wide optical absorption range from 200 to 1000 nm.[48] The increased near-infrared absorption ability as well as its high photothermal efficiency and non-toxicity, render $CuCo_2S_4$ thiospinels promising candidates for photothermal therapy (PTT) applications.[49,50] In addition, the optical bandgap for $CuCo_2S_4$ have estimated to be in the range of about 1.4-1.7 eV, depending on the morphology and the synthetic method.[51–53] Therefore, due to its desirable semiconductor properties, $CuCo_2S_4$ has found use in various photocatalytic processes.[52–54]

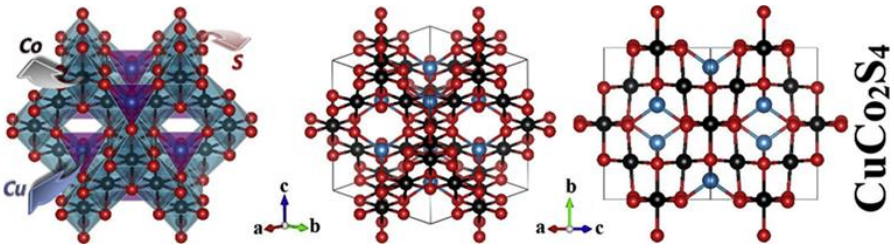

Figure 3: Crystal structure examples of the ternary thiospinel $CuCo_2S_4$.[5]

Moreover, temperature (*T*) dependent electrical resistivity (ρ) measurements in the range of 323–723 K have shown that $CuCo_2S_4$ has a metallic conductivity ($\partial\rho/\partial T > 0$), with a high carrier concentration due to its metallic nature. Also, the positive Seebeck coefficient (S) indicated a p-type carrier conduction.[55] Because of these interesting electronic and electrical properties, $CuCo_2S_4$-based materials have already been examined as promising electrode materials for high-performance supercapacitors[56,57] and other electrocatalytic processes. According to the latter, several studies have demonstrated that $CuCo_2S_4$ nanostructures are active electrocatalysts for the hydrogen evolution reaction (HER)[44], the oxygen evolution reaction (OER)[39,40], as well as for the overall water splitting[58–60]. Nevertheless, despite the progress made so far, more research into $CuCo_2S_4$-based materials for improved electrocatalytic water splitting is needed.

1.2 Transition metal phosphides

Several non-noble metals have been developed during the past few decades, whereas first row transition metals (TM), including Ni, Co, Fe, and Cu, as well as their compounds, are commonly acknowledged. The transition metal compounds that are based on the chalcogen group (group 16 of the periodic table), such as the transition metal oxides (TMOs), transition metal sulfides (TMSs), transition metal selenides (TMSes) and transition metal tellurides (TMTes), have demonstrated their finest scientific applications. However, these chalcogenide-based TMs have some major shortcomings, such as corrosion and instability. Transition metal phosphides (TMPs), which exhibit outstanding characteristics and are both affordable and corrosion resistant, have recently demonstrated better activity when compared to other TM-based materials. The earliest mention of TMPs dates back to 1792, however despite being suppressed for over 200 years (until the 1960s), their uses have since been expanded rapidly to include metallurgy, photocatalytic degradation, lithium-ion batteries, insecticides and many other.[61,62] Afterwards, it has been shown that TMPs can exhibit extraordinary activity in the

domains of photocatalytic hydrogen evolution, oxygen evolution, overall water splitting, and electrocatalytic hydrogen evolution reaction.[62,63] TMPs with the general formula M_xP_y are mostly produced via solvothermal method or solid state reaction by combining metallic or semi-metallic elements with phosphorus in different ratios. These materials are typically categorized based on the metal to phosphorus ratio. In general, there are two main types of TMPs, the metal-rich or stoichiometric metal phosphides (e.g., Ni_2P, Fe_2P, CoP) and the phosphorus-rich metal phosphides (e.g., NiP_2, SiP_2). The composition of TMPs governs both the crystal structure and the type bonding between the constituent elements. The stability of TMPs is mostly influenced by the amount of phosphorus present.

1.2.1 Nickel phosphide (Ni_2P)

Among various TMPs, nickel phosphide has been widely investigated and it has been reported that it has the ability for efficient water splitting. It comes in a variety of phases, including nickel phosphides rich in metals (Ni_2P and Ni_3P) and nickel phosphides rich in phosphorus (NiP_2, NiP_3). Metal-rich nickel phosphides at low P/Ni ratio and their composites have demonstrated superior activity toward OER, whereas phosphorus-rich nickel phosphides or metal-rich nickel phosphides with higher P/Ni atomic ratio and their composites have proven to be good catalysts for HER and photocatalytic water splitting reactions.[64,65] In the case of the Ni_2P, certain deviations have been observed. Specifically, despite being a part of the metal-rich materials, Ni_2P has been used effectively in both HER and OER applications. This is because due to the existence of well-defined exposed facets (Figure 4), Ni_2P catalyst exhibits very good catalytic activity towards HER.[66,67] Furthermore, various crystal structures are obtained by different nickel phosphide phases. Ni_3P, for instance, has a tetragonal structure, while Ni_2P adopts a hexagonal lattice (Figure 4).[68] In order to explore the chemical bonding and stability of different nickel phosphides, the heat of formation per atom of seven different Ni_xP_y phases, including Ni_3P, Ni_5P_2, $Ni_{12}P_5$, Ni_2P, NiP_2 and NiP_3, has been examined. These results indicated that as the P content increased from Ni_3P, Ni_5P_2, $Ni_{12}P_5$, to Ni_2P, the stability of the crystal structure mainly remains constant. However, it began to decline at P/Ni ratio of 4:5, and it continued to decline above 2:1 P/Ni atomic ratio in NiP_2 and Ni_3P materials. In general, these findings proved that the metal-rich Ni_2P is more stable than the other Ni_xP_y phases because it has a strong metallic and a partially ionic Ni-P bond. Comparatively, phosphorus-rich NiP_2 is less stable than Ni_2P because the stable Ni-Ni metallic bond is replaced by the less stable P-P bond, which actually reduces the overall negative enthalpy of formation. As an outcome, Ni-

rich Ni_2P is more corrosion resistant in air than its phosphorus rich counterparts. Additionally, by modifying the reaction conditions (solvent, reaction time and temperature) or the quantity and concentration of precursor materials, such as Ni sources and Ni:P molar ratio, different types of nickel phosphide phases with a diverse set of particle sizes and morphologies can be obtained.[68] In this thesis, we focus mainly on the Ni_2P TMP as an effective co-catalyst for hydrogen and oxygen evolution reactions.

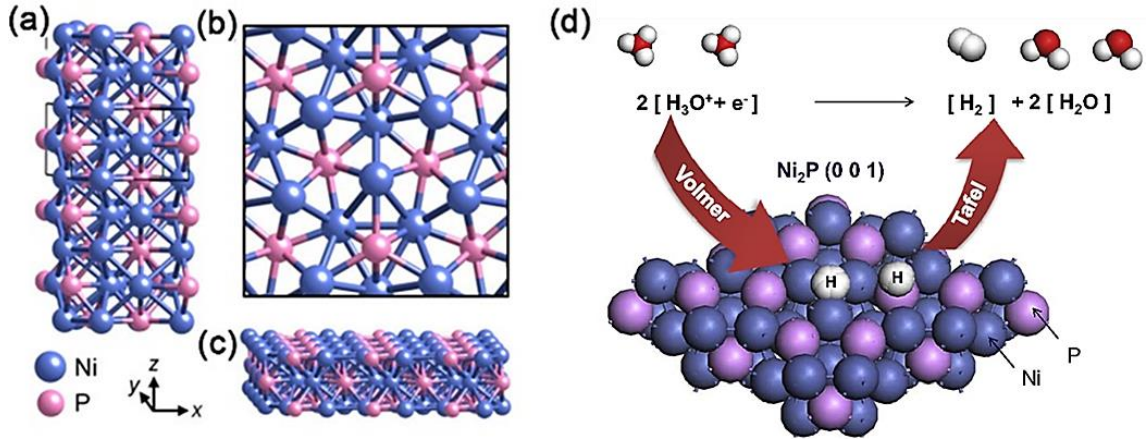

Figure 4: (**a**) Hexagonal crystal structure of Ni_2P: four-unit cells stacked on top of one another, with a single unit cell outlined, (**b**) top-down view of the Ni_2P (001) surface and (**c**) two-dimensional slice of Ni_2P showing the (001) surface on top[67]. **(d)** Hydrogen production representation over the (001) exposed facets of Ni_2P catalyst[66].

1.3 Basics of HER, OER and overall water-splitting reaction

1.3.1 Theoretical background

Due to its high energy density and absence of carbon constituents, hydrogen (H_2) is considered as a type of green fuel with high chemical-to-energy conversion efficiency that has the potential to meet the world's growing energy demands and to address the growing environmental problem caused by the use of fossil fuels.[31] Steam reforming, the traditional method for the production of H_2, is an unsustainable process that promotes the emission of the greenhouse CO_2 gas as by-product. Yet, it continues to constitute the main technology for the majority of worldwide industrial H_2 production.[30] Inversely, water electrolysis can be performed with a variety of renewable energy resources (such as wind, solar, etc.), making it a sustainable and eco-friendly method of producing high-purity H_2. The half-cell reactions of the electrochemical water splitting are the oxygen evolution reaction (OER) on the anode and the hydrogen evolution reaction (HER) on the cathode. The theoretically thermodynamic equilibrium potential (TEP, E^{θ}) of the overall water electrolysis is 1.23 V. However, in fact, a

greater operating potential much above the TEP is frequently needed to overcome the reaction energy barriers because of the slow kinetics; the difference between the applied potential and TEP is referred to as the overpotential (η).[68,69] The overpotential must be small, hence effective electrocatalysts are necessary to be developed. Although Ir-/Ru-based oxides and metal electrodes containing Pt offer the best performance so far for OER and HER, respectively, their wide-spread use is severely constrained by their high price and unavailability.[70] It is therefore highly interesting to investigate high-performance OER/HER catalysts devoid of precious metals. Since the first work on complete water electrolysis in 1789, significant developments have been made in the design and construction of numerous water-splitting electrocatalysts manufactured from earth-abundant elements.[71] So far, various electrocatalysts have been used for the two half-reactions separately in various electrolytes due to the different reaction steps and intermediate products associated with the OER and HER processes.[70,72,73] For example, transition-metal oxides, hydroxides, phosphates etc., function well for OER, while transition-metal carbides, nitrides, chalcogenides and phosphides show best activities toward HER.[74–78] More significantly, although these OER catalysts often achieve high activity in basic environment, the majority of the available HER electrocatalysts consistently demonstrate good behavior at acidic conditions.[73,79] Such a circumstance would result in electrolytes on the anode and cathode of the electrolyzer being mismatched, further complicating the manufacture of water-splitting electrolyzer cells. Consequently, electrocatalysts with both OER and HER functionality that may concurrently operate effectively in the same electrolyte solution are highly desired in order to reduce the manufacturing processes of the water-splitting device and minimize the fabrication cost.

1.3.2 General mechanisms for water splitting

The overall water splitting is regarded as a relatively simple chemical reaction with the general equation: $2H_2O \rightarrow 2H_2 + O_2$ (Equation 1.3). As we mentioned earlier, this reaction fundamentally contains two half-reactions taking place almost at the same time, the OER and HER at the anode and cathode, respectively (Equations 1.4–1.7). Theoretically, the water electrolysis reaction and the separate OER and HER half-reactions require the thermodynamic equilibrium potential (E^{θ}) of 1.23, 1.23, and 0 V (pH 0), respectively.[80] Of note, though the water-splitting reaction seems rather straightforward (the water molecules are split into O_2 and H_2), yet the two separate half-reactions (OER and HER) proceed through different pathways/mechanisms and can occur in diverse media with differed pH values.[81,82] The detailed reaction mechanisms for different half-reactions in acidic and alkaline electrolytes are

represented in Tables 2 and 3. Generally, the electrocatalytic OER operates as a complicated four-step four-electron oxidation process, which contains three surface-adsorbed intermediate products, that are OOH*, O* and OH* species (see Table 2). [81] In particular, in neutral and alkaline media, four hydroxyl (OH^-) ions are oxidized into one O_2 molecule and two water molecules, whereas in acidic solution two water molecules are oxidized into one O_2 molecule and four hydrogen (H^+) ions (Table 2).

Table 2: The detailed reaction mechanisms of OER in neutral, alkaline and acidic solutions.

Steps	**In neutral/alkaline solutions**	**In acidic solutions**
Overall	$4OH^- \rightarrow 2H_2O + O_2 + 4e^-$	$2H_2O \rightarrow 4H^+ + O_2 + 4e^-$
Step 1	$OH^- + * \rightarrow OH^* + e^-$	$H_2O + * \rightarrow OH^* + H^+ + e^-$
Step 2	$OH^- + OH^* \rightarrow O^* + H_2O + e^-$	$OH^* \rightarrow O^* + H^+ + e^-$
Step 3	$OH^- + O^* \rightarrow OOH^* + H_2O + e^-$	$O^* + H_2O \rightarrow OOH^* + H^+ + e^-$
Step 4	$OH^- + OOH^* \rightarrow H_2O + O_2 + * + e^-$	$OOH^* \rightarrow H^+ + O_2 + * + e^-$

Table 3: The detailed reaction mechanisms of HER in neutral, alkaline and acidic solutions.

Steps	**In neutral/alkaline solutions**	**In acidic solutions**
Overall	$2H_2O + 2e^- \rightarrow H_2 + 2OH^-$	$2H^+ + 2e^- \rightarrow H_2$
Volmer reaction	$H_2O + * + e^- \rightarrow H^* + OH^-$	$H^+ + * + e^- \rightarrow H^*$
Heyrovsky reaction	$H_2O + e^- + H^* \rightarrow H_2 + OH^-$	$H^+ + e^- + H^* \rightarrow H_2$
Tafel reaction	$H^* + H^* \rightarrow H_2$	$H^* + H^* \rightarrow H_2$

Compared to the OER reaction, HER involves a two-step process associated with only two electron transfer.[82] In particular, under neutral or alkaline conditions, two water molecules are reduced into one H_2 molecule and two hydroxyl ions[82], while in acidic solution, two H^+ ions are directly reduced and combined into one H_2 molecule (see Table 3).[82] During the reaction steps, H^* is the only surface-adsorbed intermediate. The reduction of water molecules or H^+ ions is first initiated to produce H^* species, which is named as Volmer reaction, followed by reaction of H^* with one water molecule (Heyrovsky reaction) or direct combination of two adjacent H^* (Tafel reaction) to form hydrogen (Table 3). [82] Under neutral or alkaline condition, hydrogen is formed by water molecules, while in acidic electrolytes hydrogen ions act as the proton source.

<u>Overall:</u>

$$2H_2O \rightarrow 2H_2 + O_2 \quad E^\theta = 1.23\ V \tag{1.3}$$

OER:

$2H_2O \rightarrow 4H^+ + O_2 + 4e^-$ (in acidic electrolyte) $E^\theta = 1.23$ V (1.4)

$4OH^- \rightarrow 2H_2O + O_2 + 4e^-$ (in neutral electrolyte) (1.5)

HER:

$2H^+ + 2e^- \rightarrow H_2$ (in acidic electrolyte) $E^\theta = 0$ V (1.6)

$2H_2O + 2e^- \rightarrow H_2 + 2OH^-$ (in neutral electrolyte) (1.7)

1.3.3 Performance metrics of electrocatalysts

i. Overpotential (η)

As mentioned earlier, the standard reduction potential of HER is defined as 0 V vs standard hydrogen electrode (SHE) at pH 0. The difference in absolute value between zero and the onset potential of the HER on an electrocatalyst is known as the overpotential (η). To reach the same current density (mA cm^{-2}), an electrocatalyst with a lower overpotential needs less energy. Depending on the polarization of electrode, the overpotential can be primarily divided into activation overpotential and concentration overpotential. If a proper electrocatalyst is used, both overpotentials can be significantly decreased. The fundamental cause of the concentration overpotential is the differential in ion concentrations between the electrode surface and bulk solution, which is caused by the slow diffusion rate of ions. However, because of the presence of a diffusion layer, stirring can only partially lower the concentration overpotential, which could then interrupt the electrode response. Resistance overpotential often referred to as junction or series overpotential. It is a significant overpotential that develops at the electrode's surfaces and interfaces. The measured electrode overpotential is larger than the thermodynamic potential due to additional voltage drop caused by the resistance along the interfaces. In this case, IR correction to obtain accurate electrocatalyst overpotential is a practical way. In a three-electrode cell, the resistance overpotential is mostly caused by the resistance between the working electrode and the reference electrode; this resistance is the R in the IR compensation. Many electrochemical work stations can measure the R value directly or the R value can be estimated from the Nyquist plots at the high frequency regime. The IR compensation is expressed by the following equations:

$$E_{correction} = I \times R \quad (1.8)$$

$$E_{corrected} = E_{uncorrected} - E_{correction} = E_{uncorrected} - (I \times R) \quad (1.9)$$

where, E is the applied potential and I is the current flowing through the system.

According to the equations 1.9, the IR correction affects slightly on the onset overpotential because the current density is quite small at that point. However, with increasing the current intensity, both the $E_{correction}$ and the shift of the polarization curves will become more pronounced.[83]

ii. Tafel slope and exchange current density

Tafel slope indicates the intrinsic catalytic property of an electrocatalyst. In practice, it is obtained from the slope of the linear part of Tafel curves:

$$\eta = b \log(j/j_0) \quad (1.10)$$

where, η is the overpotential, j is the current density and j_0 is the exchange current density.
In particular, the Tafel slope can be obtained by replotting the current density vs. potential curves into the overpotential vs. log|current density| form and fitting the linear parts of these plots to the Tafel equation (eq. 1.10). The lower value of Tafel slope indicates that a smaller overpotential is required to achieve the same current density, which suggests a faster charge transfer kinetic.

iii. Hydrogen bonding energy

A good HER electrocatalyst should typically have a free energy of hydrogen adsorption (ΔG_{H^*}) that is close to zero.[84] Considering that the normal hydrogen electrode potential is zero, a highly active HER electrocatalyst should have a hydrogen bonding Gibbs free energy that is almost equal to zero. The poor adsorption makes it harder for the proton and electrocatalyst to combine. Strongly adsorbed H_{ads} species, on the other hand, will be challenging to remove from the catalytic surface. As a result, the catalyst becomes inactive because the active sites on the surface are constantly binded. Usually, the hydrogen adsorption Gibbs free energy is obtained by DFT calculations. The Sabatier volcano can be found by plotting the exchange current density (j_0) versus the Gibbs free energy of hydrogen adsorption (ΔG_{H^*}). Better HER activity may be seen in an electrocatalyst which j_0 and ΔG_{H^*} values are situated nearer the volcano's peak (Figure 5). [85]

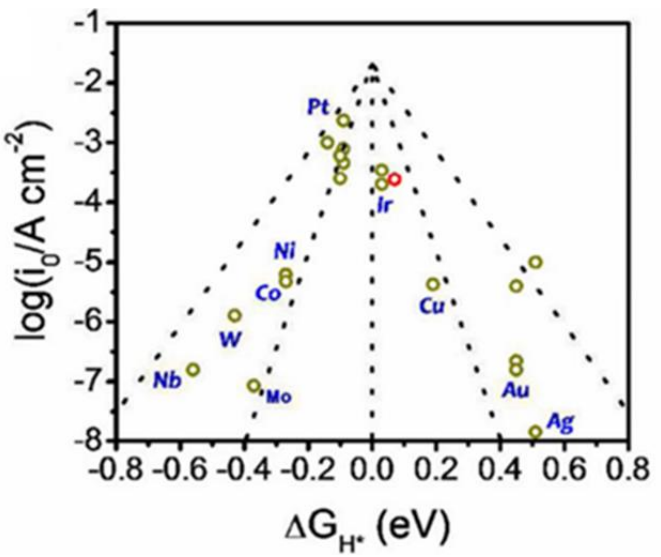

Figure 5: An illustration demonstrating the relationship between the current density (log i_0/A cm^{-2}) and the ΔG_{H*} as a volcano plot.[86]

iv. Stability

Another important factor that characterizes an electrocatalyst and a catalyst in general is the stability. Galvanostatic/potentiostatic electrolysis and cyclic voltammetry (CV) are the two common methods used to measure catalytic stability. Potential cycles, including the onset HER potential, are repeated in CV plots. The less the overpotential changes over a large number of CV cycles, the more stable the electrocatalyst is. According to voltammograms, a stable polarization curve should vary slightly compared to the original one over many CV cycles. The time-dependence of the potential (or current density) at constant current density (or overpotential) of an electrocatalyst is another method for stability study and it is known as galvanostatic (or potentiostatic) electrolysis. A current density of 10 mA cm^{-2} is often used in this kind of measurements, because this value is the most frequently used standard in HER electrocatalysis and solar fuel production. In galvanostatic electrolysis, a stable potential indicates stronger stability and it might range from a few to several hours.[83]

2. Overview and Purpose of Thesis

The general focus of this master thesis is to study new electrocatalysts for the water splitting and hydrogen evolution reaction. In this work, chapter 1 gives an overview of the general characteristics of various electrocatalysts used for HER and explaining the key concepts of electrocatalysis and water splitting. The most important findings and conclusions from the recent literature in the field are highlighted and discussed. Chapter 3 includes the analysis of

the experimental methods and instrumentation that have been used throughout this work. In chapter 4, the synthetic procedures for the preparation of catalysts studied in this work are described in detail. The aim of this thesis is to present an inexpensive, fast and eco-friendly route for the synthesis of thiospinel-based catalysts (namely $CuCo_2S_4$) modified with nickel phosphide (Ni_2P) co-catalyst, with the scope to improve the electrocatalytic activity of $CuCo_2S_4$ for hydrogen and oxygen evolution reaction. Finally, in Chapter 5, all the results from the materials' characterization (using XRD, TEM, EDS and UV-vis spectroscopy) and catalytic studies are presented and thoroughly discussed. As mentioned in the introduction, common active electrocatalysts used so far for HER and OER applications suffer from scarce and expensive materials and complicated synthetic processes employed for their production. So, the main target of this work is to examine the combination of two earth-abundant electrocatalysts, the thiospinel $CuCo_2S_4$ and nickel phosphide (Ni_2P), towards the development of efficient heterojunctional catalysts ($Ni_2P/CuCo_2S_4$) for HER and OER in alkaline solutions. Moreover, the electronic structure and charge transfer dynamics in these composite catalysts are discussed based on theoretical DFT calculations and experimental electrochemical data.

3. Experimental Methods

3.1 Chemicals and materials

Copper(II) nitrate trihydrate ($Cu(NO_3)_2 \cdot 3H_2O$, 99.5%), nickel(II) chloride hexahydrate ($NiCl_2 \cdot 6H_2O$), cobalt(II) nitrate hexahydrate ($Co(NO_3)_2 \cdot 6H_2O$, 99.5%), thiourea (CH_4N_2S, 99%), ethylenediamine ($C_2H_8N_2$) and red phosphorus were purchased from Sigma Aldrich. Double distilled water was used in all experiments. Absolute ethanol and isopropanol (99%) were procured from Fischer Scientific Company. All chemicals were used as received without any further purification.

3.2 Synthesis of Electrocatalysts

3.2.1 Synthesis of $CuCo_2S_4$ nanosheets

The $CuCo_2S_4$ catalyst was synthesized using a simple hydrothermal method.[87] In particular, $Cu(NO_3)_2 \cdot 3H_2O$ and $Co(NO_3)_2 \cdot 6H_2O$ precursors with a molar ratio of 1:2 were firstly dissolved in 30 ml of distilled (DI) water. After stirring the solution for 10 min, 8 mmol of thiourea was added and the solution was further stirred for another 15 min. Then, 2 ml ethylenediamine was added into this solution and the obtained mixture was transferred to a 100 ml Teflon lined autoclave. The autoclave was sealed and kept at 200 ^{o}C for 12h. The obtained black powder

product was isolated by centrifugation and washed three times with DI water and ethanol. The product was dried at 60 ^{o}C for 6h and stored for further studies.

3.2.2 Synthesis of Ni_2P-decorated $CuCo_2S_4$ catalysts

Ni_2P nanoparticles were directly deposited on the $CuCo_2S_4$ surface by a hydrothermal method. Briefly, 50 mg of as-prepared $CuCo_2S_4$ nanosheets and appropriate amounts of $NiCl_2$ and red phosphorus with a molar ratio of 1:5 were dispersed in 10 ml of DI water. After stirring for about 10 min, the suspension was transferred to a 50 ml Teflon lined autoclave and filled with DI water (30 ml). The autoclave was sealed and kept at 150 ^{o}C for 24h and the obtained black product was isolated by centrifugation and washed three times with DI water and ethanol. The product was dried at 60 ^{o}C for 6h and stored for further studies. The $NiCl_2$ and red phosphorus concentration was varied in the reaction mixture to give a series of $Ni_2P/CuCo_2S_4$ composites with different loadings of Ni_2P, i.e., 15, 20, 30 and 40 wt.%.

3.2.3 Synthesis of Ni_2P and $P/CuCo_2S_4$

For comparison purposes, we also prepared pure Ni_2P microparticles and a P-modified $CuCo_2S_4$ (labeled as $P/CuCo_2S_4$) sample. The Ni_2P was synthesized using the same hydrothermal method for the synthesis of $Ni_2P/CuCo_2S_4$ composites, but without the presence of $CuCo_2S_4$. In precise, $NiCl_2$ and red phosphorus with a molar ratio of 1:5 were dispersed with stirring in 40 ml of DI water and the obtained suspension was transferred to a 50 ml Teflon lined autoclave and kept at 150 ^{o}C for 24 h. For the synthesis of $P/CuCo_2S_4$, the same procedure as for the 30% Ni_2P-loaded $CuCo_2S_4$ was followed but without the addition of $NiCl_2$ in the reaction mixture. In particular, 50 mg of as-prepared $CuCo_2S_4$ and appropriate amount of red phosphorus (corresponding to the amount used for the synthesis of 30% $Ni_2P/CuCo_2S_4$) were dispersed in 40 ml DI water and the mixture was transferred to a 50 ml Teflon lined autoclave and kept at 150 ^{o}C for 24 h. For both samples, the obtained black powder products after the hydrothermal reaction were isolated by centrifugation and washed three times with DI water and ethanol. Finally, the products were dried at 60 ^{o}C for 6h and stored for further use.

3.3 Structural characterization

For the purpose of this study, X-ray diffraction (XRD) was performed on a Panalytical X'pert Pro MPD instrument with Cu-Kα radiation (λ = 1.5418 Å), operated at 45 kV and 40 mA. Energy-dispersive X-ray spectroscopy (EDS) was performed on a JEOL JSM 6390 LV scanning electron microscope (SEM) equipped with an Oxford INCA PentaFETx3 detector

(Oxfordshire, UK). Transmission electron microscopy (TEM) measurements were performed with a JEOL JEM-2100 instrument (LaB_6 filament) operating at 200 kV. The samples were prepared by dispersing fine powders in ethanol using sonication and then drop-casting on a holey carbon-coated Cu grid. X-ray photoelectron spectroscopy (XPS) was conducted on a SPECS spectrometer using a Phoibos 100 1D-DLD electron analyzer and Al Kα radiation as the energy source (1486.6 eV). Binding energy values were corrected with reference to the C 1s (284.8 eV) signal of adventitious carbon. UV–vis diffusion reflectance spectra were recorded with a Shimadzu UV-2600 spectrophotometer, using $BaSO_4$ powder as a 100% reflectance reference. The diffuse reflectance data were transformed to absorbance with the Kubelka–Munk function: $\alpha/S = (1-R)^2/(2R)$, where R is the measured reflectance and α and S are the absorption and scattering coefficients, respectively.

3.4 Electrochemical measurements

Electrochemical tests were performed using a single-channel potentiostat/galvanostat Princeton Applied Research VersaSTAT 4 equipped with a three-electrode cell, consisting of a sample-coated carbon plate working electrode, an Ag/AgCl (saturated KCl) reference electrode, and a Pt-mesh counter electrode. To fabricate the working electrodes, a catalyst ink was made by dispersing 10 mg of each sample in 0.5 mL dimethylformamide (DMF). Then, 20 μL Nafion solution (5 wt.%) was added and the mixture was ultrasonicated for 15 min and left under stirring for 24 h. When a uniform suspension was formed, 40 μL of the solution was drop-casted on a carbon plate substrate (effective surface 1 cm^2) and the film was dried at 40–50 °C for 1h and then heated at 120 ºC for 1h before electrochemical tests.

Polarization (J–V*)* curves, CV curves, Mott–Schottky plots and electrochemical impedance spectroscopy (EIS) Nyquist plots were measured in a 1M KOH electrolyte (pH=14). The polarization curves were recorded by using linear sweep voltammetry (LSV) at a 5 mV s^{-1} scan rate and all the measured potential was manually corrected by iR compensation and converted into the reversible hydrogen electrode (RHE) at pH=0 according to the Nernst equation:

$$E_{RHE} = E_{Ag/AgCl} + 0.197 + 0.059 \times pH \quad (1.11)$$

where $E_{Ag/AgCl}$ is the measured potential versus Ag/AgCl.

The polarization curves were replotted as overpotential (η) versus the logarithm of current density (log |J|) to obtain Tafel plots. For the estimation of the electrochemically active surface area (ECSA), the double-layer capacitance (C_{dl}) was determined from the cyclic voltammetry (CV) curves, recorded in a potential range where no Faradaic process occurs, using different

scan rates from 5 to 50 mV s^{-1}. EIS Nyquist measurements were performed over a frequency range from 10 kHz to 0.1 Hz at the potential of −1.3 V (vs Ag/AgCl, saturated KCl) with an AC perturbation of 10 mV. In Nyquist plots, the EIS data were fitted using ZView software to an equivalent Randles circuit model, consisted of an electrolyte resistance (R_s), a charge transfer resistance (R_{ct}) and a constant phase element (CPE) to account for the nonideality of the frequency dispersion in the capacitance response. For the Mott-Schottky plots, the space-charge capacitance (C_{SC}) of the electrode/electrolyte interface was measured at 1 kHz with a 10 mV AC voltage amplitude, and the obtained flat-band potentials were converted to the reversible hydrogen electrode (RHE) scale using equation (1-11). The carrier density (N_A) of the as-prepared materials was estimated from the slope of the linear portion of the Mott-Schottky plots, according to the Mott–Schottky equation:

$$N_A = C_{SC}^2 \cdot 2 \cdot (E - E_{FB}) / \varepsilon \cdot \varepsilon_0 \cdot e_0 \quad (1.12)$$

where, C_{SC} is the space charge capacitance, E_{FB} is the flat band potential, E is the applied potential, N_A is the carrier density of the electrode material, ε is the dielectric constant of the electrode material, ε_0 is the vacuum permittivity (8.8542×10^{-14} F cm^{-1}), e_0 is the elementary charge (1.602×10^{-19} C), and the term $(E-E_{FB}) \cdot C_{SC}^2$ is the reciprocal of the slope of the Mott–Schottky plot.

The electrochemical stability of the prepared catalysts was tested by chronopotentiometry measurements at a constant current density of 10 mA cm^{-2} for 72 h. The overall water-splitting tests were conducted in a home-made two-electrode system using 1M KOH electrolyte (pH=14).

3.5 Theoretical calculations

Density functional theory (DFT) calculations were performed using the projector augmented wave method (PAW) and the generalized gradient approximation (GGA) of Perdew-Burke-Ernzerhof (PBE) for exchange-correlation functional as implemented by Vienna *ab initio* simulation package (VASP). Plane wave expansion was limited at 450 eV cut-off energy. Ionic motion was converged at 0.01 eV/A^2 and for the electronic part at 10^{-5} eV. We used a 5 x 5 x 1 Monkhorst-Pack mesh for the first Brillouin zone sampling.

4. Results and Discussion

4.1 Structural and morphological characterization

The chemical composition of the pristine and Ni_2P-modified $CuCo_2S_4$ samples was confirmed with energy dispersive X-ray spectroscopy (EDS). All the EDS spectra showed the presence of Cu, Co and S elements with an average Cu:Co:S atomic ratio of ~0.99:2:4.34, which is very close to the stoichiometry of $CuCo_2S_4$. The slightly increased amount of sulfur in samples is due to the excess amount of sulfur precursor (thiourea) used for the synthesis, which probably form a S-passivation layer on the surface of $CuCo_2S_4$. As for the Ni_2P content, it was determined by EDS data on the basis of the Ni to Co atomic ratio, and was found to be similar to the nominal composition of the catalysts (within ~0.5 wt.% deviation), see Table 4. Moreover, for comparison purposes, we also prepared a P-modified $CuCo_2S_4$ sample (labeled as P/$CuCo_2S_4$), using the same synthetic process as for the 30% $Ni_2P/CuCo_2S_4$ catalyst but without the addition of $NiCl_2$ in the reaction. EDS analysis on this sample gave a Cu:Co:S ratio of ~1.01:2:4.24, in line with the $CuCo_2S_4$ stoichiometry, and a P-loading amount of about 28 wt.%, confirming the incorporation of phosphorus into the $CuCo_2S_4$ structure.

Table 4. Elemental composition of the as-prepared $CuCo_2S_4$, $Ni_2P/CuCo_2S_4$ and P/$CuCo_2S_4$ samples according to EDS analysis.

Material	Cu (at.%)	Co (at.%)	S (at.%)	Ni (at.%)	P (at.%)	Ni_2P content (wt.%)
$CuCo_2S_4$	13.30	26.95	59.75	-	-	-
15% $Ni_2P/CuCo_2S_4$	9.50	19.24	39.75	7.02	24.49	14.9
20% $Ni_2P/CuCo_2S_4$	8.37	19.03	46.63	9.86	16.11	19.9
30% $Ni_2P/CuCo_2S_4$	9.57	18.27	37.85	15.97	18.34	29.5
40% $Ni_2P/CuCoS_4$	8.32	15.89	33.12	21.73	20.94	39.6
P/$CuCo_2S_4$	8.78	17.44	36.97	-	36.82	

The crystal structure of the $CuCo_2S_4$ and $Ni_2P/CuCo_2S_4$ materials was characterized by powder X-ray diffraction (XRD). The XRD pattern (Figure 6) of as-prepared $CuCo_2S_4$ show typical diffraction peaks related to the cubic spinel structure of $CuCo_2S_4$, according to the JCPDS card no. 42-1450. After the in-situ growth of Ni_2P on $CuCo_2S_4$, several additional diffraction peaks appear in the XRD patterns of $Ni_2P/CuCo_2S_4$ composites, which can be assigned to the hexagonal Ni_2P (JCPDS card no. 74-1385). The broad XRD peaks observed for Ni_2P suggest small crystallite size; an average crystal size of ~20 nm is derived by Scherrer's equation. From Figure 6, it is apparent that with the increment of Ni_2P loading, the intensity

of the $CuCo_2S_4$ diffraction peaks gradually decreases, while the intensity of the Ni_2P XRD peaks becomes stronger, especially in samples with the highest Ni_2P-loading levels (i.e., 30 and 40 wt.% Ni_2P), suggesting a significant coverage of the $CuCo_2S_4$ surface by Ni_2P particles. Despite that, the in-situ hydrothermal synthesis of the $Ni_2P/CuCo_2S_4$ heterostructures seems to have no obvious influence on the crystal structure of $CuCo_2S_4$ starting material. Therefore, from XRD data it can be concluded that the desired $CuCo_2S_4$ thiospinel structure and the respective $Ni_2P/CuCo_2S_4$ crystal heterostructures have been successfully prepared.

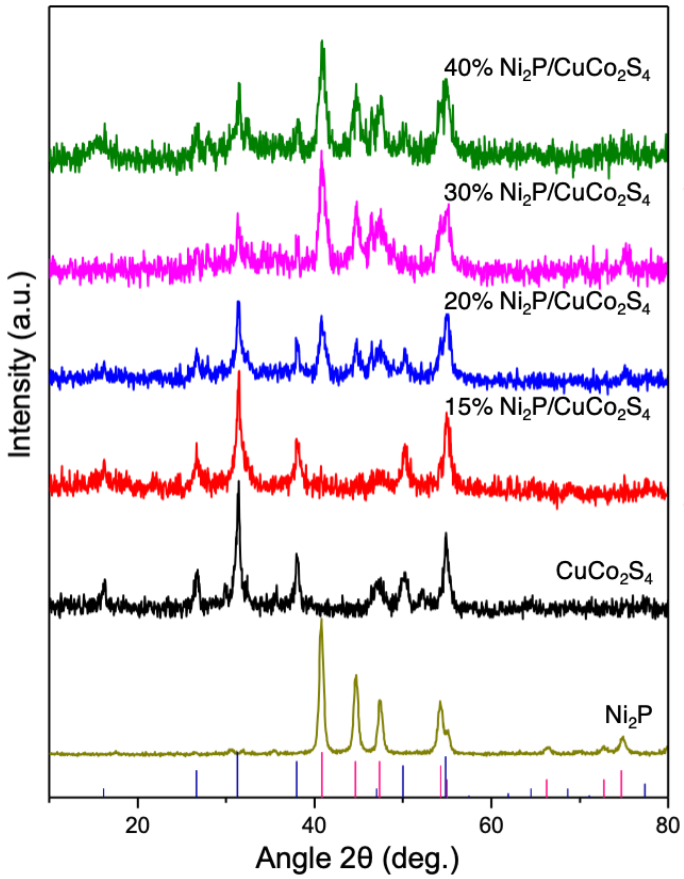

Figure 6: XRD patterns of $CuCo_2S_4$ and $Ni_2P/CuCo_2S_4$ catalysts. The JCPDS powder diffraction standards of $CuCo_2S_4$ and Ni_2P are also given.

Transmission electron microscopy (TEM) and selected-area electron diffraction (SAED) were employed to gain a thorough insight into the morphology and crystal structure of the as-prepared materials. Representative TEM images for the $Ni_2P/CuCo_2S_4$ composite containing 30 wt.% Ni_2P, which is the most active catalyst in this study, are shown in Figures 7a and b. Figure 7a is a low magnification TEM image, where a nanosheet-like morphology can be seen. This image also reveals that the microstructure contains $CuCo_2S_4$ nanosheets with a lateral size of ~50 nm that are randomly agglomerated, forming an interconnected network. Also, some

particles of Ni_2P with a diameter of ~10-15 nm (appeared as dark areas in Figures 7a and b) can be distinguished on the surface of the $CuCo_2S_4$. More importantly, the small-sized Ni_2P particles are attached on the surface of $CuCo_2S_4$ nanosheets and, in fact, with a tight contact as shown in high-resolution TEM (HRTEM) image (Figures 7b). The HRTEM image illustrates lattice fringes with interplanar distances of 5.4 Å and 3.4 Å that can be assigned to the (111) facets of cubic $CuCo_2S_4$[40] and (0001) facets of hexagonal Ni_2P, respectively, further confirming that the Ni_2P nanoparticles are growth on the $CuCo_2S_4$ surface and crucially, with intimate contact which is beneficial for the interfacial charge transfer within the heterostructure. Besides, the SAED pattern collected from a small area of the composite structure shows a series of Debye−Scherrer diffraction rings (Figure 7c), coinciding with the crystal planes of cubic Fd-3m $CuCo_2S_4$ (yellow lines) and hexagonal P-62m Ni_2P (green lines), in line with the HRTEM and XRD analysis.

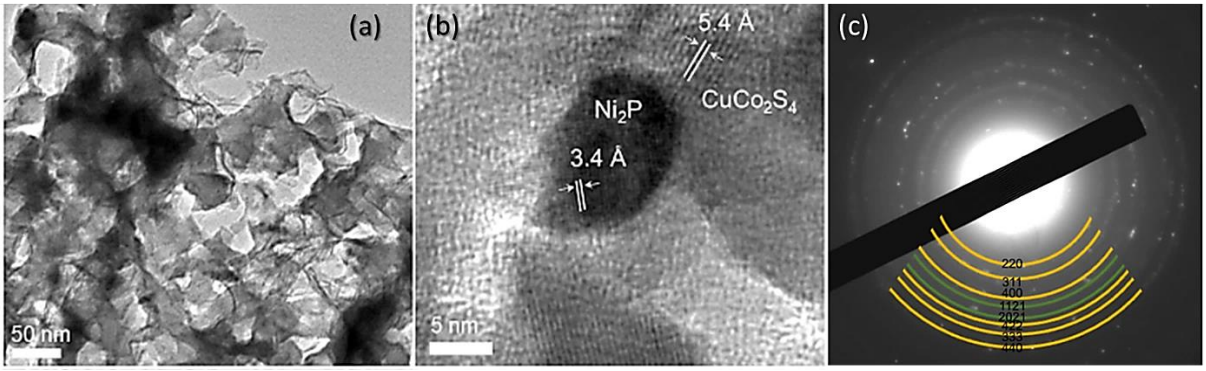

Figure 7: (a) Typical TEM image, displaying the agglomerated nanosheet-like morphology of the 30% $Ni_2P/CuCo_2S_4$ catalyst. (b) High-resolution TEM (HRTEM) of an isolated Ni_2P nanoparticle in intimate contact with $CuCo_2S_4$ nanosheets. (c) SAED pattern taken from a small area of the 30% $Ni_2P/CuCo_2S_4$ structure, showing the diffraction rings of cubic Fd-3m $CuCo_2S_4$ (yellow lines) and hexagonal P-62m Ni_2P (green lines).

The surface chemical state of elements in pristine and 30% Ni_2P-loaded $CuCo_2S_4$ sample was examined by X-ray photoelectron spectroscopy (XPS). The high-resolution Cu 2p, Co 2p and S 2p XPS spectra and the corresponding Auger Cu LMM signal of $CuCo_2S_4$ are illustrated in Figures 8a-c. In the deconvoluted Cu 2p XPS spectrum (Figure 8a), the peaks at binding energies of 932.6 and 952.6 eV are attributed to Cu $2p_{3/2}$ and Cu $2p_{1/2}$ core levels of Cu(I), respectively. Meanwhile, the small peaks at 933.8 and 954.5 eV binding energy can be ascribed to the Cu $2p_{3/2}$ and Cu $2p_{1/2}$ states of Cu(II). The presence of small amount of Cu(II) in $CuCo_2S_4$ is also corroborated by the weak satellite peak at 942.7 eV, which is indicative of the existence of paramagnetic Cu(II) ions. Further evidence for the prominent existence of C(I) ions in the $CuCo_2S_4$ lattice was obtained from the Auger Cu LMM spectrum (Figure 8b). It shows an

intense peak at 569.1 eV that is compatible with the binding energy of Cu(I)-S species.[88–90] The presence of both Cu(I) and Cu(II) in $CuCo_2S_4$ thiospinel has also been reported extensively in other studies.[54,91–93]

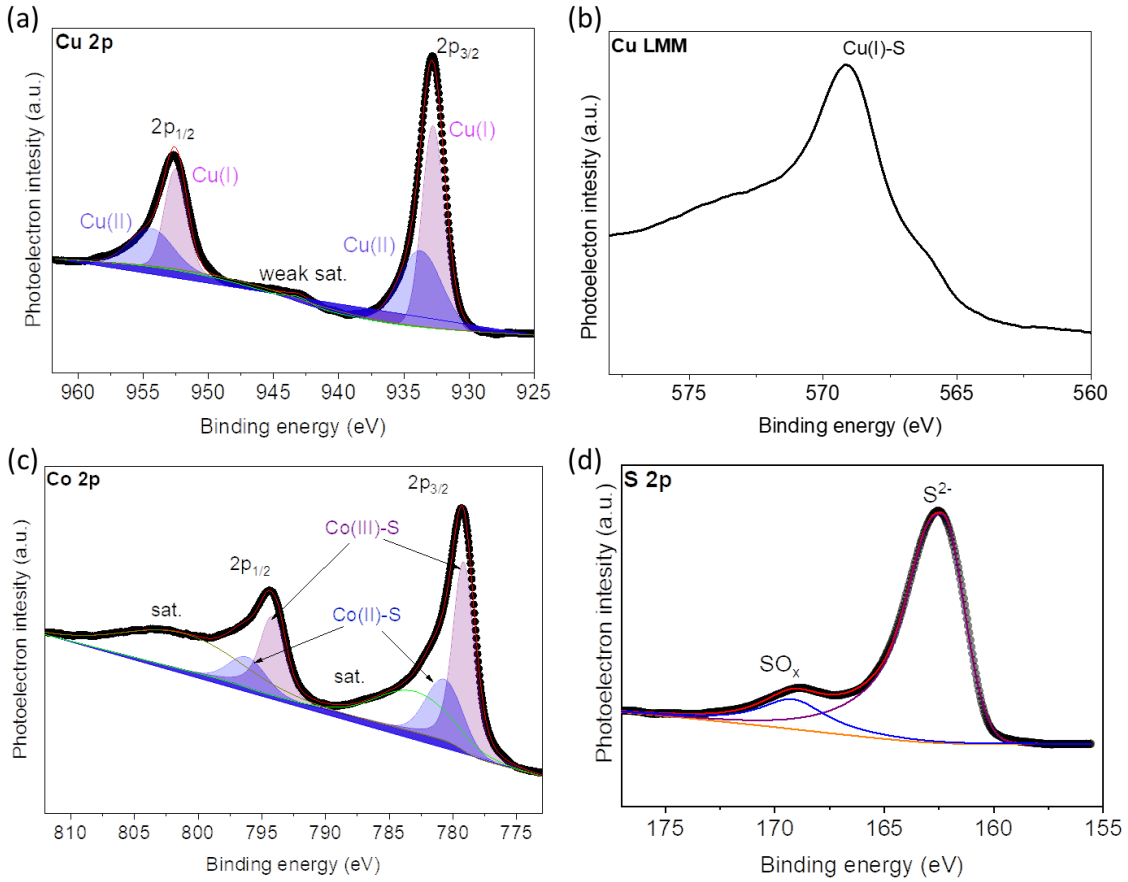

Figure 8: (a, b) High-resolution Cu 2p XPS spectrum and the corresponding Auger Cu LMM spectrum, and (c) Co 2p and (d) S 2p XPS spectra for the $CuCo_2S_4$ catalyst.

In Figure 8c, the core level spectra of Co 2p for the $CuCo_2S_4$ appear as a doublet peak centered at 779.1 and 794.2 eV, which can be ascribed to the Co $2p_{3/2}$ and Co $2p_{1/2}$ states of Co(III), respectively. Meanwhile, the weak signals at 780.9 and 796.5 eV correspond respectively to the Co $2p_{3/2}$ and Co $2p_{1/2}$ spin-orbit peaks of Co(II).[91–93] The broad features shown in the Co 2p XPS spectrum at higher binding energies are shake-up satellite peaks from Co(II) ions. These results suggest the coexistence of Co(II) and Co(III) species in the surface of $CuCo_2S_4$, although the high intensity peak of Co(III) suggests a prominent amount of Co(III) species. Additionally, the S 2p peak located at 162.4 eV corresponds to the sulfide (S^{2-}) ions of the thiospinel structure (Figure 8d), whereas the S 2p line centered at 168.6 eV indicates a minor surface oxidation (SO_x species) due to the air exposure of sample.[58,94]

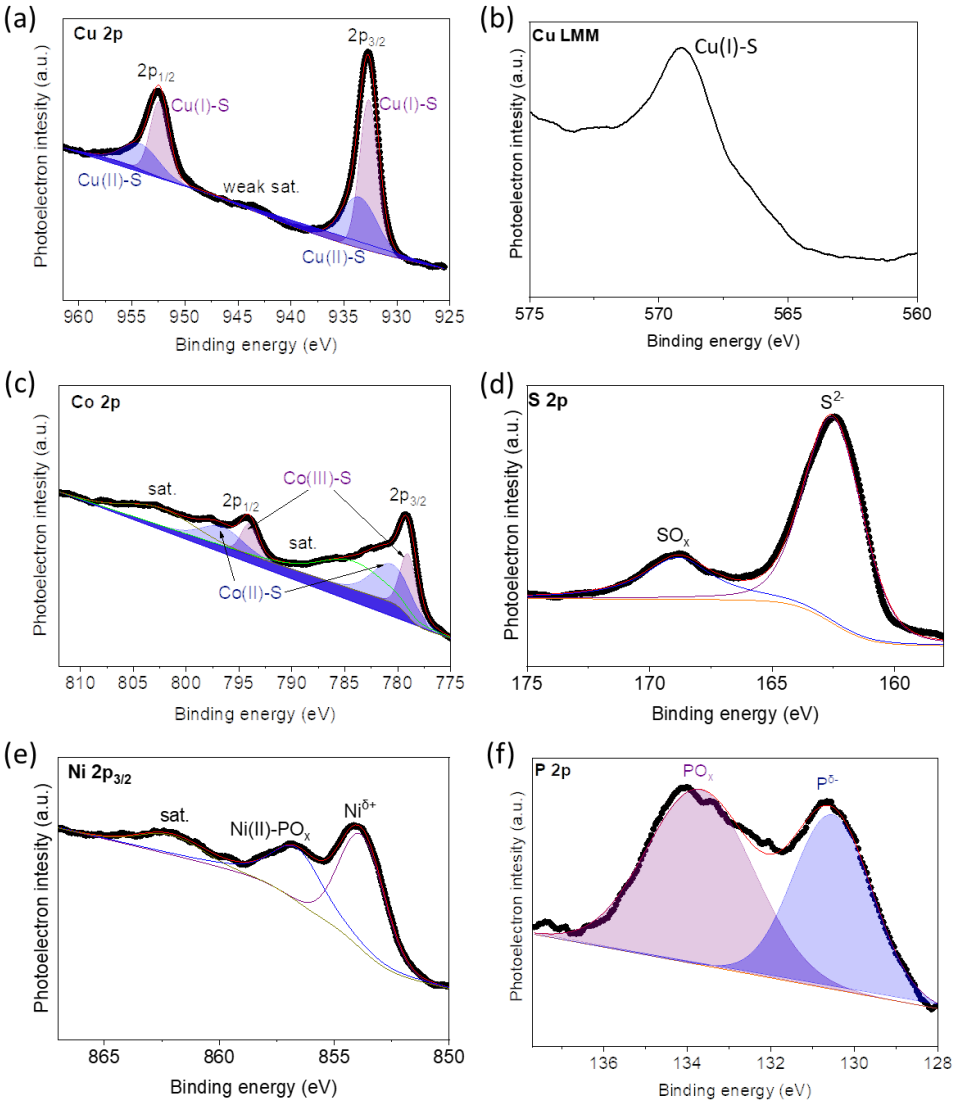

Figure 9: (a, b) High-resolution XPS spectrum of Cu 2p and the corresponding Auger Cu LMM spectrum. Core-level XPS spectra of (c) Co 2p, (d) S 2p, (e) Ni $2p_{3/2}$ and (f) P 2p for the 30% Ni_2P-modified $CuCo_2S_4$ catalyst.

For catalyst with 30 wt.% Ni_2P (30% $Ni_2P/CuCo_2S_4$), the Cu 2p, Co 2p and S 2p XPS core-level and Auger Cu LMM peaks are detected at binding energies similar to those of $CuCo_2S_4$. As shown in Figure 9a, the Cu 2p signal indicates the presence of Cu(I)-S (Cu $2p_{3/2}$: 932.7 eV, Cu $2p_{1/2}$: 952.4 eV) and Cu(II)-S (Cu $2p_{3/2}$: 933.6 eV, Cu $2p_{1/2}$: 954.1 eV, shape-up satellite: 942.6 eV) species. The Cu LMM Auger spectrum, in Figure 9b, again provides convincing evidence of the existence of Cu(I) ions on the surface of 30% $Ni_2P/CuCo_2S_4$, showing a peak at 569.1 eV. The signals of the deconvoluted Co 2p spectrum, in Figure 9c, are attributed to the Co(III) (Co $2p_{3/2}$: 779.0, Co $2p_{1/2}$: 794.0 eV) and Co(II) (Co $2p_{3/2}$: 780.5, Co $2p_{1/2}$: 796.6 eV) species, very similar to the pristine $CuCo_2S_4$ material. For the S 2p region (Figure 9d), a prominent peak at 162.5 eV due to the S^{2-} ions and a weak feature at 168.8 eV due to the

partially oxidized SO_x species are present. These results clearly indicate that the chemical nature of elements in the starting $CuCo_2S_4$ material is not affected by the hydrothermal Ni_2P modification process. As for the Ni_2P particles on the thiospinel surface, the Ni $2p_{3/2}$ signal at 853.8 eV is associated with the $Ni^{\delta+}$ species in Ni_2P and the broad feature at 856.6 eV is attributed to the partially oxidized N(II)-PO_x species on the catalyst surface (Figure 9e). In agreement to this, the P 2p XPS spectrum of composite catalyst presents a peak at 130.5 eV due to the slightly negatively charged phosphorous species ($P^{\delta-}$) in Ni_2P (as a result of the electron transfer from Ni to P) and a broad peak at around 134 eV due to the partially oxidized phosphate complexes (PO_x), see Figure 9f.[95,96] Consequently, the XPS data together with the EDS and XRD results reveal the successful deposition of Ni_2P onto the $CuCo_2S_4$ surface to form $Ni_2P/CuCo_2S_4$ heterostructures.

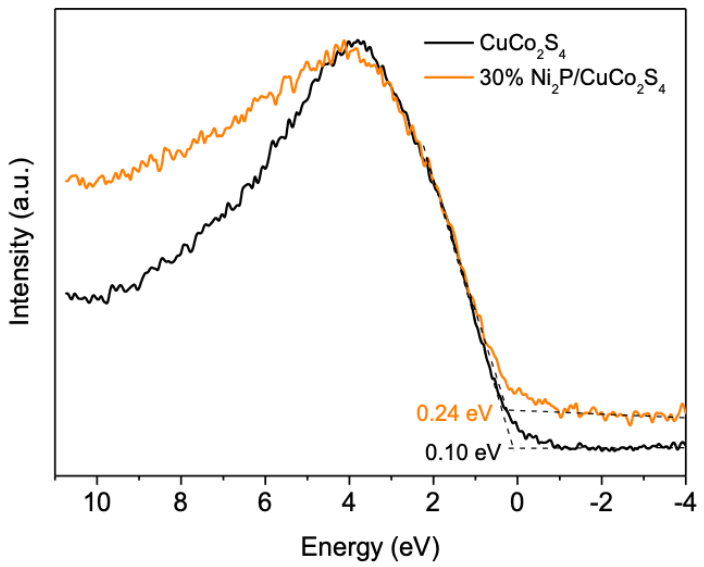

Figure 10: XPS valence band spectrum of $CuCo_2S_4$ and Ni_2P-modified catalyst (30% $Ni_2P/CuCo_2S_4$).

The valence band (VB) XPS spectra of $CuCo_2S_4$ and 30% $Ni_2P/CuCo_2S_4$ materials provide an additional hint for the strong electronic interactions between the Ni_2P and $CuCo_2S_4$ components. The $CuCo_2S_4$ shows a photoemission onset, which is defined as the energetic difference between the surface Fermi level and the VB maximum of the semiconductor, at ~0.10 eV, indicating a p-type conductivity. For the 30% $Ni_2P/CuCo_2S_4$ catalyst, the photoemission onset is measured to be ~0.24 eV (Figure 10). Consequently, the upshift of the Fermi level due to the Ni_2P deposition, as shown in Figure 10, can be corelated to the transfer of electrons from Ni_2P to $CuCo_2S_4$ until the Fermi levels of the two components become equal. Under these conditions, the flow of electric carriers generates a depletion layer (positively

charged region) in Ni_2P and an accumulation layer (negatively charged region) on the $CuCo_2S_4$ side of the $Ni_2P/CuCo_2S_4$ junction. Indeed, variations of the charge distribution at the $Ni_2P/CuCo_2S_4$ interface were also evidenced by density functional theory (DFT) computations.

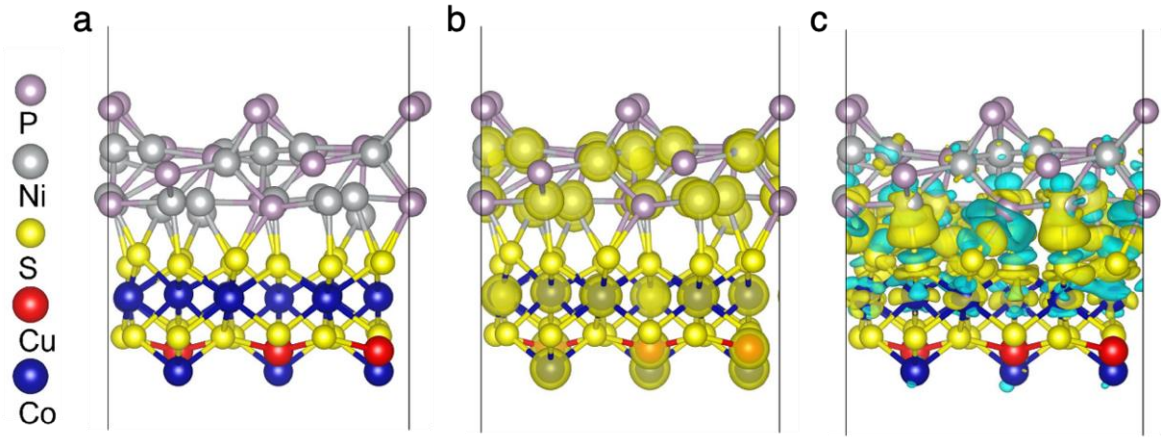

Figure 11: (a) The simulation cell, (b) the charge density and (c) the charge density difference for the $Ni_2P/CuCo_2S_4$ heterostructure.

DFT calculations were also performed to determine the charge-transfer interactions at the $Ni_2P/CuCo_2S_4$ interface. In our $Ni_2P/CuCo_2S_4$ structural model we assumed the $CuCo_2S_4$ bridges Ni_2P by its surface sulfur atoms (Figure 11a), which is a plausible option given the synthesis route to composite the catalyst, that is, in situ deposition and hydrothermal growth of Ni_2P nanoparticles on the $CuCo_2S_4$ surface. The charge density difference shown in Figure 11c was estimated by subtracting the charge densities of the isolated $CuCo_2S_4$ and Ni_2P structures from that of the $Ni_2P/CuCo_2S_4$ heterostructure seen in Figure 11b. The corresponding DFT calculations explicitly designate an interfacial electron transfer from Ni_2P to $CuCo_2S_4$, signifying a strong electronic coupling. Indeed, the $Ni_2P/CuCo_2S_4$ interface shows a strong electron charge redistribution, suggesting that the interface plays a key role in improving the electrical conductivity and, thus, the electrocatalytic behavior of the catalyst. Ideally, an efficient electrocatalyst should possess electron-rich surface-active sites so as to facilitate the initial adsorption of water via the electron-deficient H atom and the subsequent dissociation of the electron-rich OH–H bond via H transfer to the catalyst's surface.[97,98] Taken together, these DFT results and VB XPS experiments illustrate that the electron accumulation at the $Ni_2P/CuCo_2S_4$ interface due to the strong electronic coupling facilitates the destabilization of alkaline water, resulting in an improved alkaline HER.

The optical properties of the $CuCo_2S_4$ and $Ni_2P/CuCo_2S_4$ catalysts as well as those of Ni_2P microparticles were examined by ultraviolet–visible/near IR diffuse reflectance spectroscopy

(UV−vis/NIR DRS). As shown in Figure 12a, the UV−vis/NIR spectrum of $CuCo_2S_4$, transformed from the diffuse reflection data according to the Kubelka–Munk function, shows an absorption edge near ~757 nm due to the intrinsic electron transition from the valence band (VB) to the conduction band (CB) in $CuCo_2S_4$. Compared to $CuCo_2S_4$, the Ni_2P-modified materials undergo a small blue-shift (by ~7–9 nm) upon increasing the concentration of Ni_2P; they exhibit an absorption edge in the 748-750 nm range. The optical band gap (E_g) of the prepared catalysts was determined from Tauc plots for direct gap semiconductors, i.e., $(ahv)^2$ vs hv plots derived from the UV−vis/ NIR spectra, as shown in Figure 12b. Specifically, the E_g of the unmodified $CuCo_2S_4$ was estimated to be ~1.64 eV, while the band gap of $Ni_2P/CuCo_2S_4$ composites is slightly blue-shifted (by ~10–20 meV), see Table 5. For comparison, the energy gap of the as-prepared Ni_2P particles was found to be ~1.68 eV. These results suggest intense electronic interactions at the interface of $Ni_2P/CuCo_2S_4$ junction, in agreement with HRTEM, VB XPS and DFT results.

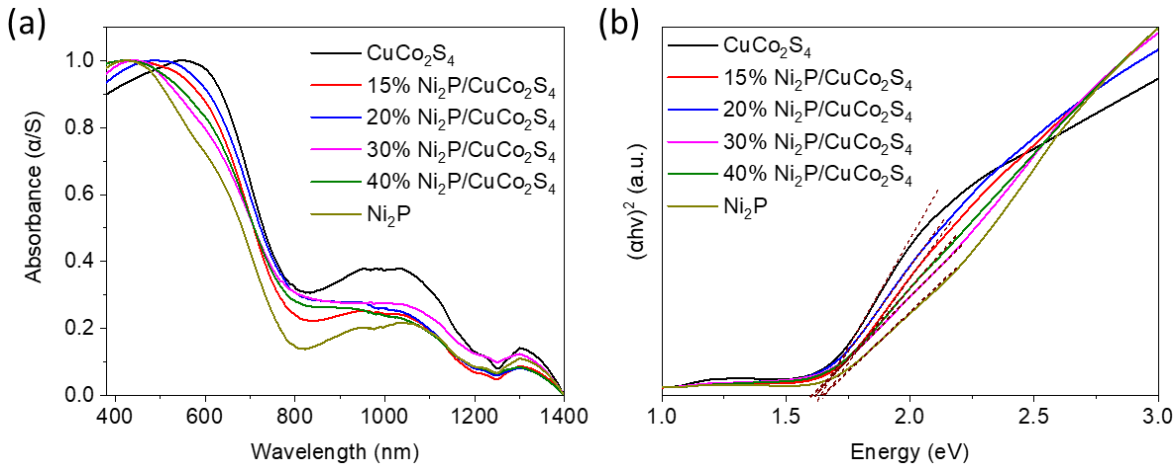

Figure 12: (a) UV−vis/NIR absorption spectra and (b) the corresponding Tauc plots of the as-prepared $CuCo_2S_4$, Ni_2P and $Ni_2P/CuCo_2S_4$ materials.

Table 5. Estimated bandgap (E_g) values obtained from Tauc plots for the $CuCo_2S_4$, Ni_2P and $Ni_2P/CuCo_2S_4$ materials.

Sample	**Bandgap, E_g (eV)**
$CuCo_2S_4$	1.64
15% $Ni_2P/CuCo_2S_4$	1.65
20% $Ni_2P/CuCo_2S_4$	1.65
30% $Ni_2P/CuCo_2S_4$	1.66
40% $Ni_2P/CuCo_2S_4$	1.66
Ni_2P	1.68

4.2 Electrocatalytic studies

The electrocatalytic HER performance of as-prepared $CuCo_2S_4$ and $Ni_2P/CuCo_2S_4$ catalysts was evaluated in 1M KOH electrolyte using a typical three electrode system, consisting of a sample-coated carbon plate working electrode (WE), an Ag/AgCl (saturated KCl) reference electrode (RE) and a Pt-mesh counter electrode (CE). Figure 13a shows the iR-corrected polarization curves (current density (J) vs. applied potential (V)) for all the prepared catalysts recorded at a scan rate of 5 mV s^{-1}. For comparison, the respective polarization curves of carbon electrode (as a blank catalyst), Pt electrode (as one of the best-known HER catalysts), and Ni_2P and P-modified $CuCo_2S_4$ ($P/CuCo_2S_4$) samples are also obtained. The measured potentials were converted to RHE at pH=0 according to equation 1.11. The Pt electrode shows an excellent electrocatalytic HER activity, requiring a very small overpotential of 48 mV at 10 mA cm^{-2}, as expected. On the contrary, the carbon plate electrode has almost negligible HER activity, which means that the carbon-plate substrate has minimal contribution to the observed activity of our catalysts. The as-prepared Ni_2P and unmodified $CuCo_2S_4$ catalysts show a rather poor HER performance with an overpotential of 400 mV and 348 mV at a current density of 10 mA cm^{-2}, respectively. Conversely, Ni_2P modification significantly improves the HER performance of $CuCo_2S_4$, and the sample with 30 wt.% Ni_2P content (30% $Ni_2P/CuCo_2S_4$) achieves the best HER performance, requiring an overpotential of only 183 mV at 10 mA cm^{-2}. With further increment of the Ni_2P content (40 wt.%), the HER activity is remarkable suppressed, as inferred by the increased overpotential value (237 mV at 10 mA cm^{-2}). For comparison, we also measured the electrocatalytic activity of the P-modified $CuCo_2S_4$ sample ($P/CuCo_2S_4$) towards HER, under the same experimental conditions. As shown in Figure 13a, $P/CuCo_2S_4$ catalyst (with a P content of ~28 wt.%) exhibits a much lower HER activity than the pristine and Ni_2P-modified $CuCo_2S_4$ catalysts, demanding an overpotential of 385 mV to afford 10 mA cm^{-2} current density. Thus, all the above results indicate that P-modification alone is not advantageous for the catalytic reactivity of $CuCo_2S_4$, whereas coupling of Ni_2P and $CuCo_2S_4$ contributes synergistically to the HER activity of the, otherwise poorly-active, single-component Ni_2P and $CuCo_2S_4$. A comparison of electrocatalytic results in Table 6 clearly confirms the high HER activity of out 30% $Ni_2P/CuCo_2S_4$.

Table 6. Electrochemical HER parameters of the measured overpotential at 10 mA cm^{-2} (η_{10}) and Tafel slopes for the Pt electrode and the prepared Ni_2P, $CuCo_2S_4$ NSs and $Ni_2P/CuCo_2S_4$ catalysts.

Material	**η_{10} (mV)**	**Tafel slope (mV dec^{-1})**
Ni_2P	400	146
$CuCo_2S_4$	348	110
15% $Ni_2P/CuCo_2S_4$	300	102
20% $Ni_2P/CuCo_2S_4$	251	98
30% $Ni_2P/CuCo_2S_4$	183	78
40% $Ni_2P/CuCo_2S_4$	237	83
Pt electrode	48	73

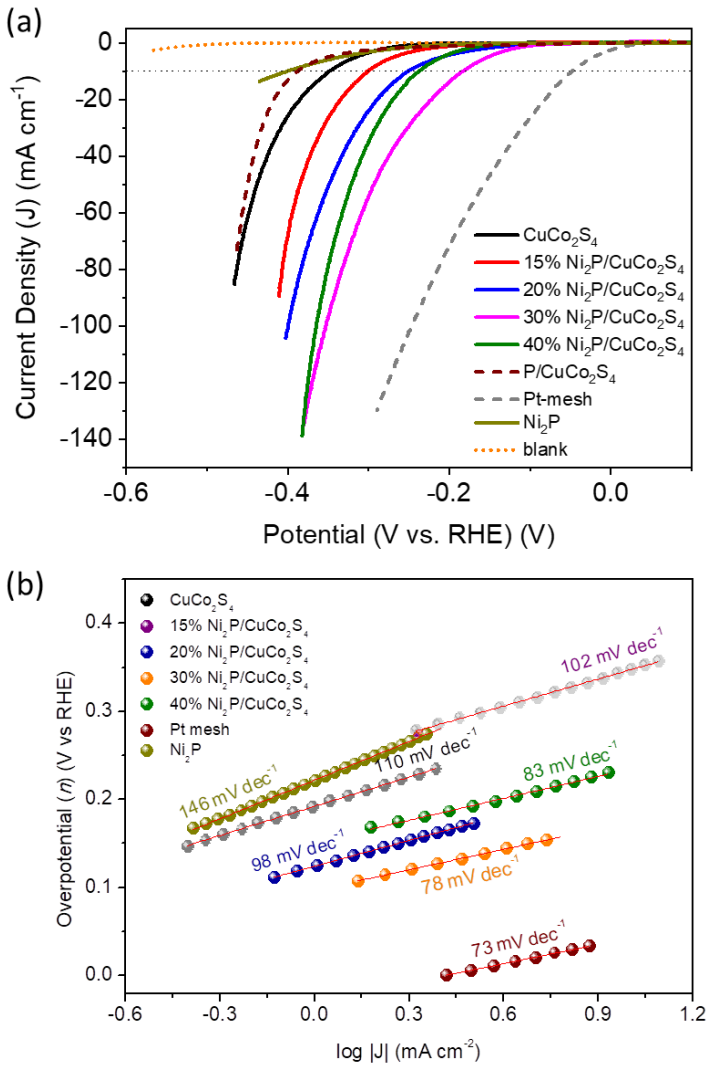

Figure 13: (a) iR-corrected polarization (LSV) curves (scan rate 5 mV s^{-1}) and (b) the corresponding Tafel plots (log |J| vs. overpotential (η)) of HER over the as-prepared Ni_2P, $CuCo_2S_4$ and P- and Ni_2P-modified $CuCo_2S_4$ catalysts in 1M KOH electrolyte. For comparison, the respective results of the carbon plate (blank) and Pt electrodes are also given. The red lines in panel b are the corresponding linear fits to the experimental data.

The superior HER activity of the prepared $Ni_2P/CuCo_2S_4$ catalysts is associated with favorable electrochemical reaction kinetics, which were evaluated by the corresponding Tafel plots analysis. Shown in Figure 13b, the Tafel plots give slopes of 146, 110, 102, 98, 78 and 83 mV dec^{-1} for the Ni_2P, $CuCo_2S_4$ and the Ni_2P-modified $CuCo_2S_4$ catalysts with 15, 20, 30 and 40 wt.% Ni_2P content, respectively (Table 6). Thus, among these materials, 30% $Ni_2P/CuCo_2S_4$ catalyst attains the smaller Taffel slope (78 mV dec^{-1}), which is comparable to that for Pt electrode (73 mV dec^{-1}), underscoring more favorable reaction kinetics. In general, a Taffel slope less than 120 mV dec^{-1} is indicative of a faster increment of HER rate with increasing overpotential and suggests a Volmer-Heyrovsky type catalytic mechanism, where the reaction of surface-adsorbed H^* intermediate species with water molecules to produce H_2 (Heyrovsky reaction) is the rate-determining step of the HER process.[99]

The catalytic activity of our best catalyst (30% $Ni_2P/CuCo_2S_4$) was also examined towards the OER in 1 M KOH solution and compared to that of the Pt electrode and $CuCo_2S_4$, Ni_2P and $P/CuCo_2S_4$ materials (deposited on carbon-plate substrate). The carbon-plate substrate was also measured as a blank reference. From the iR-corrected LSV curves, in Figure 14a, it can be seen that the Ni_2P and $CuCo_2S_4$-based materials exhibit various electron-transfer processes in the range of 1.4-1.5 V vs RHE, which can be attributed to redox reactions of cobalt and copper in the $CuCo_2S_4$[58] and possible nickel in Ni_2P[100]. Hence, as it is difficult to determine the catalytic onset potential, a current density of 40 mA cm^{-2} was used as a reference to compare the OER performance of the catalysts. As in HER experiments, the bare carbon-plate electrode showed negligible OER activity, and hence, it has a minimum contribution in the observed activity of our catalysts. Surprisingly, the Ni_2P catalyst exhibited a somewhat better OER activity than the Pt electrode, showing an overpotential of 520 mV versus 570 mV at 40 mA cm^{-2}. However, both these electrocatalysts showed poorer activities than the prepared $CuCo_2S_4$-based samples. More specifically, 30% $Ni_2P/CuCo_2S_4$ demonstrated the best OER performance with an overpotential of 360 mV at 40 mA cm^{-2}, outperforming also the $P/CuCo_2S_4$ (410 mV) and pristine $CuCo_2S_4$ (380 mV). Nevertheless, from Tafel analysis of the polarization curves (Figure 14b), $CuCo_2S_4$ gave a smaller Tafel slope (78 mV dec^{-1}) than 30% $Ni_2P/CuCo_2S_4$ (136 mV dec^{-1}) and $P/CuCo_2S_4$ (189 mV dec^{-1}), signaling faster OER kinetics over the surface of $CuCo_2S_4$ nanosheets. The electrochemical OER results for all the examined catalysts are summarized in Table 7.

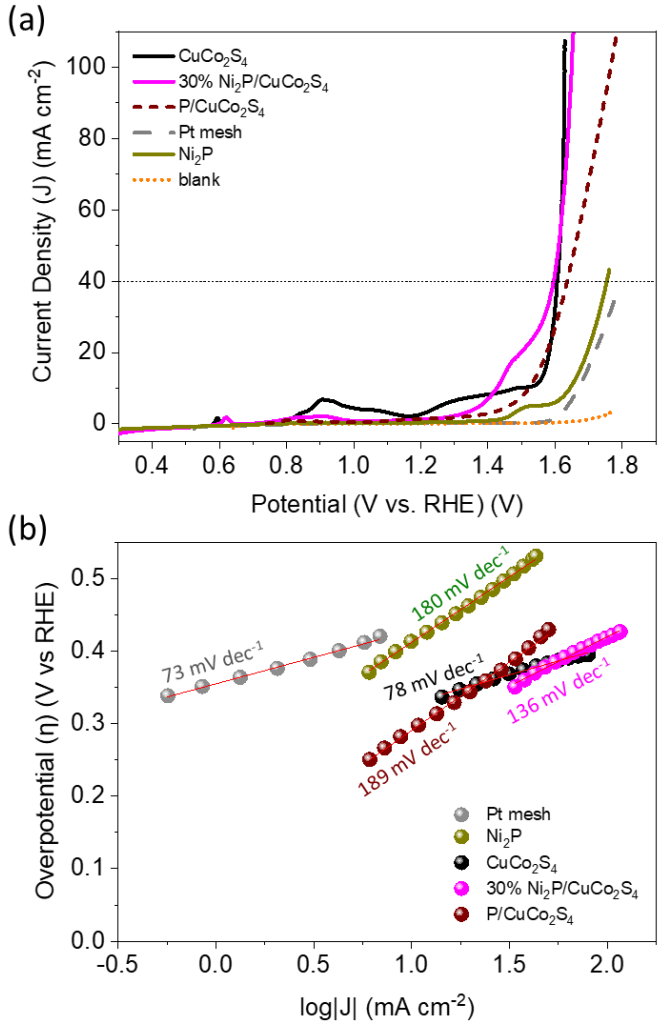

Figure 14: (a) iR-corrected polarization (LSV) curves (scan rate 5 mV s^{-1}) and (b) the corresponding Tafel plots (log |J| vs. overpotential (η)) of OER over the as-prepared Ni_2P, $CuCo_2S_4$, 30% $Ni_2P/CuCo_2S_4$ and $P/CuCo_2S_4$ catalysts in 1M KOH electrolyte. For comparison, the respective plots of the carbon plate and Pt electrodes are also given. The red lines in panel b are the corresponding linear fits to the experimental data.

Table 7. Electrochemical OER parameters for the Pt electrode and the as-prepared Ni_2P, $CuCo_2S_4$, 30% $Ni_2P/CuCo_2S_4$ and $P/CuCo_2S_4$ catalysts.

Material	**η_{40} (mV)**	**Tafel slope (mV dec^{-1})**
Ni_2P	520	180
$CuCo_2S_4$	380	78
30% $Ni_2P/CuCo_2S_4$	360	136
$P/CuCo_2S_4$	410	189
Pt electrode	570	73

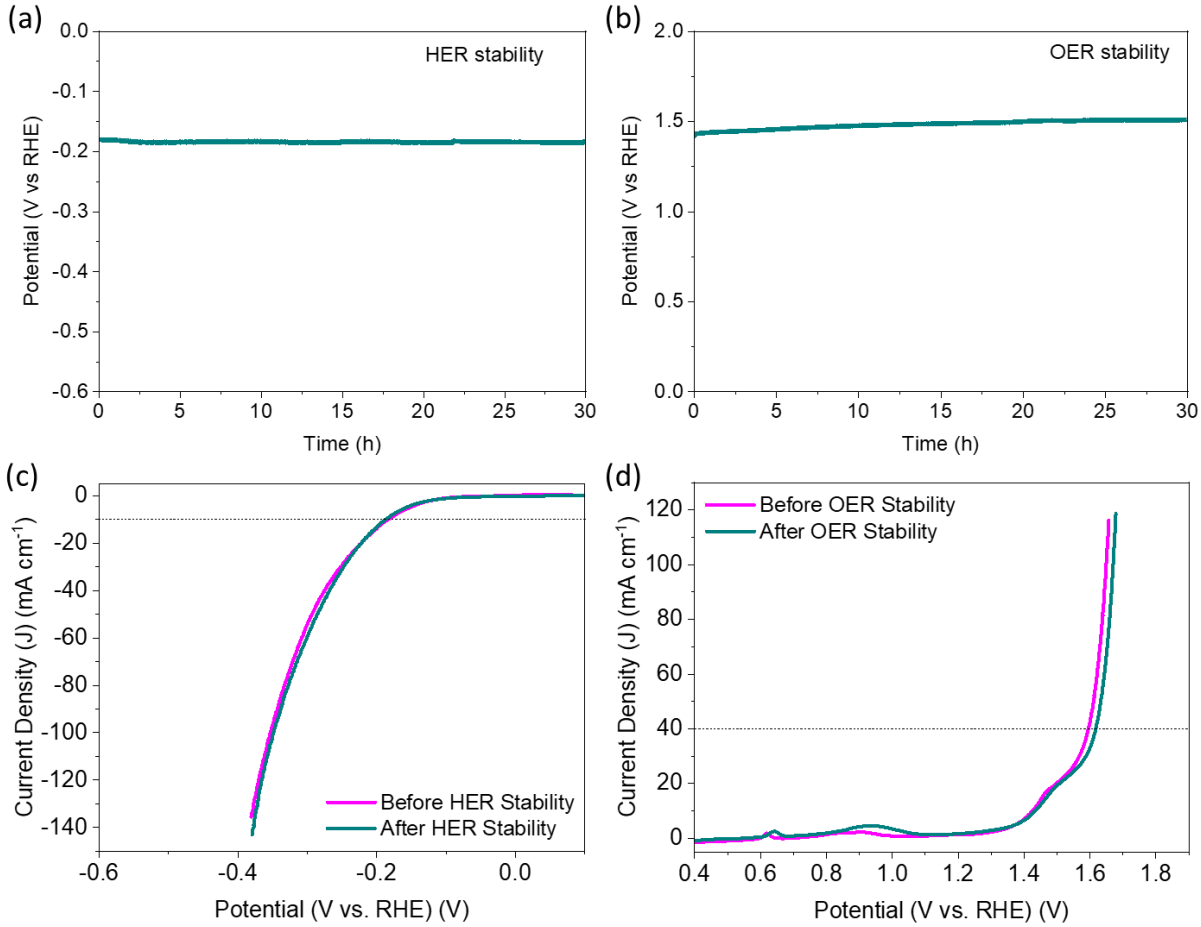

Figure 15: (a and b) Chronopotenriometric curves of HER and OER over 30% $Ni_2P/CuCo_2S_4$ catalyst at 10 mA cm^{-2}. (c and d) The corresponding HER and OER polarization curves of 30% $Ni_2P/CuCo_2S_4$ catalyst recorded before and after the stability tests.

Apart from superior electrocatalytic activity, 30% $Ni_2P/CuCo_2S_4$ catalyst exhibited also very good electrochemical stability for both HER and OER, as evidenced by chronopotentiometric measurements in 1 KOH electrolyte. Figures 15a and b show the time-dependent current-voltage curves of HER and OER, respectively, measured at a constant applied current density of 10 mA cm^{-2}. After continuous testing for 30 h, the 30% $Ni_2P/CuCo_2S_4$ catalyst did not show any significant degradation of its electrochemical activity, retaining 98% and 94% of its initial potential for HER and OER, respectively. This excellent durability of the catalyst is further supported by the corresponding HER and OER polarization curves recorded after the stability test. Shown in Figures 15c and d, the HER and OER activity of 30% $Ni_2P/CuCo_2S_4$ remains almost the same after the electrocatalytic tests, showing a HER overpotential of 187 mV at 10 mA cm^{-2} and a OER overpotential of 383 mV at 40 mA cm^{-2}, very close to the initial values of 183 and 360 mV, respectively.

Considering the catalytic activity and stability for both HER and OER, it is anticipated that the 30% $Ni_2P/CuCo_2S_4$ could operate as bifunctional electrocatalyst for overall water splitting.

To demonstrate this perspective, a two-electrode water electrolysis cell was assembled by using the 30% $Ni_2P/CuCo_2S_4$ catalyst (drop-casted on carbon plate substrate) as both cathode and anode materials in 1M KOH electrolyte. As shown in Figure 16, the 30% $Ni_2P/CuCo_2S_4$ electrode system manifests a good overall water-splitting activity, requiring a small onset potential of 1.67 V and a cell voltage of 1.78 V to achieve a current density of 10 mA cm^{-2}.

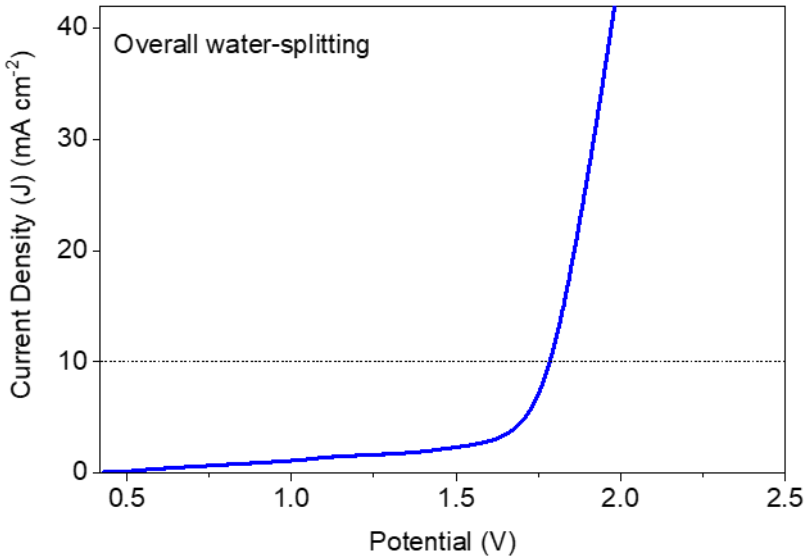

Figure 16: Polarization curve (without iR compensation) for overall water splitting measured in 1 M KOH electrolyte at a scan rate of 5 mV s^{-1} using a two-electrode cell with 30% $Ni_2P/CuCo_2S_4$ operating as both anode and cathode materials.

4.3 Role of Ni_2P on the electrocatalytic activity

In general, the effectiveness of an electrocatalyst is largely associated with the catalytically active surface area and charge transfer dynamics at the electrode/electrolyte interface. In this respect, the apparent superior activity of Ni_2P-modified catalysts was further evaluated by means of electrochemically surface area (ECSA). The ECSA is a critical parameter in assessing the intrinsic activity of electrocatalysts, as it gives information about the accessible surface area of an active catalyst for electrochemical reactions. The ECSA can be determined from the double layer capacitance (C_{dl}) and the specific capacitance (C_s) of an electrode material according to Equation 1.13[101]:

$$ECSA = C_{dl}/C_s \tag{1.13}$$

When an electrode surface is subjected to a voltage ramp, a steady-state capacitive current is observed. At non-faradaic region, the only process taking place within the voltage range is the charging of the double layer, that is, movement of ions on either side of the electrode/electrolyte

interface. For ideal capacitors, the measured current (I_c) is related to the double layer capacitance and the scan rate (ν) by the following equation[102] :

$$I_c = \nu \cdot C_{dl} \tag{1.14}$$

On this basis, a common method for obtaining C_{dl} consists in collecting cyclic voltammograms (CV) under different scan rates within a potential region where no redox processes take place. The C_{dl} is then obtained as a slope of the linear plot I_c against ν. Here, the I_c values were extracted from the CV curves of catalysts (drop-casted on FTO substrates) recorded in 1M KOH electrolyte at a potential window of 0.22–0.42 V vs RHE, using various scan rates of 5, 10, 20 and 50 mV sec^{-1}.

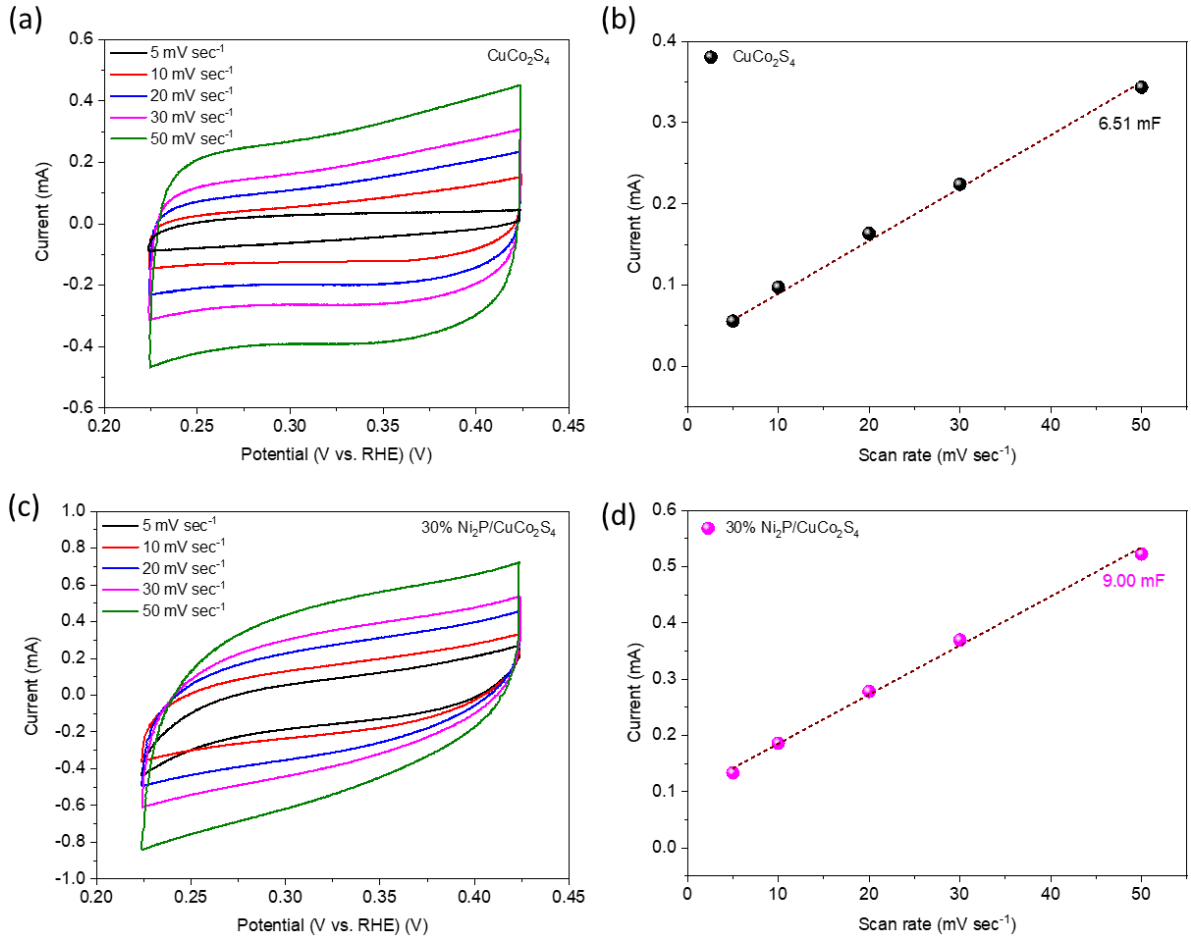

Figure 17: (a, c) Non–faradaic CV curves measured between 0.22 and 0.42 V vs RHE at various scan rates and (b, d) current vs scan-rate plots, where the current (I_c) values are extracted from the anodic and cathodic scans of CV curves at 0.325 mV applied potential for the pristine and 30 wt.% Ni_2P-modified $CuCo_2S_4$ electrocatalysts.

Figures 17a and c show the non-faradaic CV curves, while Figures 17b and d show the corresponding I_c vs. ν plots for the pristine and 30 wt.% Ni_2P-modified $CuCo_2S_4$ catalysts,

respectively. The calculated data show that the 30% $Ni_2P/CuCo_2S_4$ has a C_{dl} of 9.00 mF, which is 1.4 times the C_{dl} of the unmodified $CuCo_2S_4$ (6.51 mF) under the same conditions. Considering a C_S of 40 μF cm^{-2}, which is a typical value for bare FTO substrate in alkaline media[103], a ECSA of ~225 cm^2 was estimated for 30% $Ni_2P/CuCo_2S_4$ versus to ~163 cm^2 for $CuCo_2S_4$, which is directly corelated to the higher electrocatalytic activity of 30% $Ni_2P/CuCo_2S_4$. So, it became clear that the in-situ growth of Ni_2P nanoparticles on the $CuCo_2S_4$ surface leads to a significant increment in surface-active sites available to reactions, and thus to more favorable electrochemical reaction kinetics.

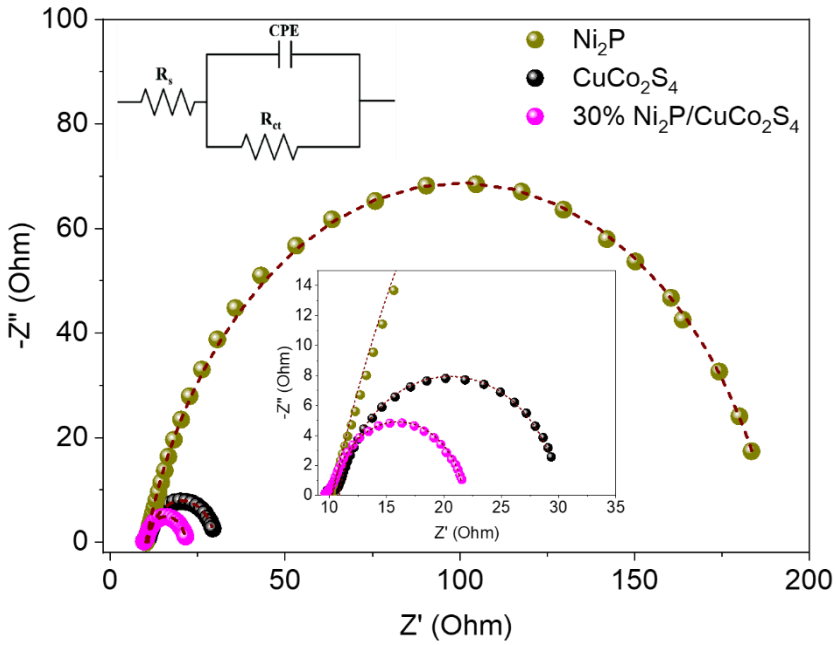

Figure 18: EIS Nyquist plots (inset: equivalent Randles circuit model used to simulate the impedance data) of the as-prepared Ni_2P, $CuCo_2S_4$ and 30% $Ni_2P/CuCo_2S_4$ catalysts. The inset graph is a magnification of the Z' vs -Z'' plots in the region 10–35 Ω for clarity.

The charge-transfer kinetics at the interface between the electrolyte and the prepared catalysts were characterized by electrochemical impedance spectroscopy (EIS) and Nyquist plot measurements. The EIS was performed in 1M KOH electrolyte over a frequency range of 0.1 Hz –10 kHz using an applied potential of -1.3 V vs Ag/AgCl (saturated KCl) and under the influence of an AC perturbation of 10 mV. Figure 18 shows the Nyquist plots for the Ni_2P, $CuCo_2S_4$ and the 30 wt.% Ni_2P-modified $CuCo_2S_4$ catalysts (drop-casted on FTO substrate). All the EIS data were fitted using a simple Randles equivalent circuit model, as illustrated in Figure 18 (inset), in order to determine the charge-transfer resistance (R_{ct}) of each catalyst. The simulated results confirm that the single-component Ni_2P exhibits the largest R_{ct} value (~180 Ω), which explains its sluggish reaction kinetics, as revealed by the Tafel analysis. On the

contrary, 30% $Ni_2P/CuCo_2S_4$ catalyst has the lowest R_{ct} resistance (~11.5 Ω), which is almost 1.8 times lower than that of unmodified $CuCo_2S_4$ (~20.6 Ω), corroborating its superior electrocatalytic performance. The estimated R_{ct} values of the examined catalysts are reported in Table 8. Taken together, the ECSA and EIS Nyquist results affirm that, besides the larger electrochemically active surface area that provides more surface-reaching charge channels, deposition of Ni_2P nanoparticles on the $CuCo_2S_4$ surface also induce a smoother and more efficient charge transfer effect at the interface.

To acquire a clearer picture of the effect of heterojunction formation and charge transfer mechanism in the $Ni_2P/CuCo_2S_4$ HER activity, Mott−Schottky analysis was also performed at a fixed AC frequency of 1 kHz in 1 M KOH electrolyte (pH = 14). The Mott−Schottky (M-S) plots and the corresponding fits of the linear portion of the inverse square space-charge capacitance vs applied potential (Csc^{-2} vs. V) curves for pure Ni_2P as well as the $CuCo_2S_4$ and 30% $Ni_2P/CuCo_2S_4$ samples are shown in Figure 19. All potentials were converted from Ag/AgCl electrode to RHE scale using equation (1-11). From the M-S plots, the corresponding flat-band (E_{FB}) potentials of the examined samples were estimated from the extrapolated straight lines at $Csc^{-2} = 0$ and the results are listed in Table 8. From Figure 19a, it is apparent that the as-prepared Ni_2P exhibits a positive linear slope, representing typical n-type conductivity, i.e., electrons are the majority carriers. Also, the E_{FB} of Ni_2P was found to be -0.1 V vs RHE, which is slightly above the thermodynamic potential of water reduction (0 V vs RHE). On the other hand, the negative slope observed in the M-S curves of the unmodified $CuCo_2S_4$ indicates a p-type conductivity and its E_{FB} was estimated to be 1.56 V vs RHE. These results suggest that, during the growth of Ni_2P nanoparticles on the $CuCo_2S_4$ surface, a p-n junction is formed at their interface, causing an electron flow from Ni_2P to $CuCo_2S_4$ until the Fermi levels are aligned. The net effect of this process is anticipated to drive the E_{FB} of the $Ni_2P/CuCo_2S_4$ heterostructure to a more negative (cathodic) potential compared to the pristine $CuCo_2S_4$. Indeed, from M-S plot, the E_{FB} of 30% $Ni_2P/CuCo_2S_4$ heterostructure is catholically shifted to 1.43 V vs RHE, while maintaining its p-type conductivity, as inferred from the negative slope of the M-S curve. These results are in very good agreement with the theoretical DFT and experimental VB XPS data.

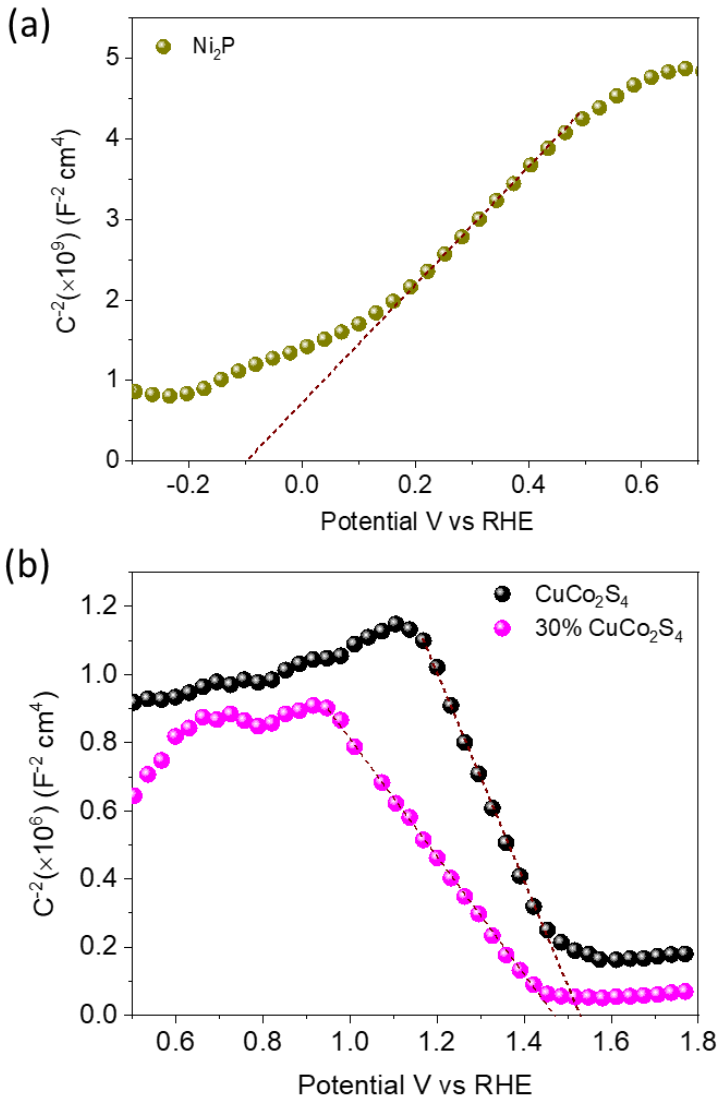

Figure 19: Mott−Schottky plots (C_{SC}^{-2} as a function of applied potential vs RHE at pH 0) for the as-prepared (a) Ni_2P and (b) $CuCo_2S_4$ and 30% $Ni_2P/CuCo_2S_4$ catalysts. Dashed lines are fit to the experimental data.

Table 8. Electrochemical data obtained from EIS Nyquist and Mott−Schottky measurements for the as-prepared Ni_2P, $CuCo_2S_4$ and 30% $Ni_2P/CuCo_2S_4$ catalysts.

Sample	**E_{fb} (pH=0) (V vs RHE)**	**Carrier Density (cm^{-3})**	**R_{ct} (Ohm)**
Ni_2P	-0.10	5.3×10^{17}	180
$CuCo_2S_4$	1.56	1.2×10^{21}	20.6
30% $Ni_2P/CuCo_2S_4$	1.43	2.2×10^{21}	11.5

Based on the estimated E_{FB} potentials and optical bandgaps (as determined from UV–vis/NIR absorption spectra), a reasonable energy band diagram for each catalyst is constructed and presented in Figure 20a. Here we assumed that the E_{FB} is related to the CB and VB edge

position at the liquid/semiconductor interface for n-type and p-type semiconductors, respectively. In order to further elucidate the charge transfer mechanism in the formed $Ni_2P/CuCo_2S_4$ heterojunction, the free-carrier charge density of the examined Ni_2P, $CuCo_2S_4$ and 30% $Ni_2P/CuCo_2S_4$ samples were calculated from the slopes of the M-S plots, using Equation 1.12 and assuming a dielectric constant (ε) of 3.75 for our materials[54]; the obtained charge densities are compared in Table 8. The results showed that the donor density of n-type Ni_2P is 5.3×10^{17} cm^{-3}, while the acceptor density of p-type $CuCo_2S_4$ is 1.2×10^{21} cm^{-3}. After Ni_2P modification, the acceptor density of the 30% $Ni_2P/CuCo_2S_4$ heterostructure raises to 2.2×10^{21} cm^{-3}, which is almost double that of unmodified sample, probably as a consequence of the efficient charge-carrier separation at the interface of $Ni_2P/CuCo_2S_4$ junction. Therefore, the combined results from DFT, VB XPS and Mott-Schottky analysis explicitly confirm strong interface electronic interactions and coupling between n-type Ni_2P and p-type $CuCo_2S_4$.

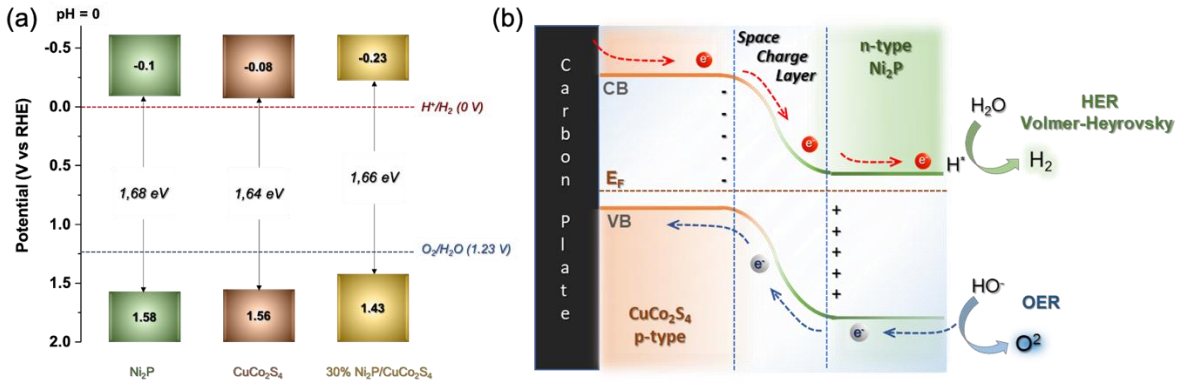

Figure 20: (a) Energy band diagrams for Ni_2P, $CuCo_2S_4$ and $Ni_2P/CuCo_2S_4$ catalysts. (b) Schematic representation of the electrocatalytic mechanism over the $Ni_2P/CuCo_2S_4$ heterojunction.

Thanking into account all above considerations, a schematic representation of the electrocatalytic mechanism over the $Ni_2P/CuCo_2S_4$ heterojunction is proposed in Figure 20b. Briefly, in HER catalysis, the flow of charge carriers at the p-n junction generates a depletion layer (positively charged region) in Ni_2P side and an accumulation layer (negatively charged region) on the $CuCo_2S_4$ side of the $Ni_2P/CuCo_2S_4$ heterostructure with a strong built-in potential, as evidenced by DFT calculations and VB XPS spectra. This may facilitate a smooth transfer of electrons from the electrode back-contact to the junction interface, where they are consumed by the adsorbed H* species and produce H_2 at a faster rate. Oppositely, on the anode side, the strong space charge layer at the $Ni_2P/CuCo_2S_4$ junction favors the efficient transfer of electrons from OH^- (in alkaline electrolyte) to the VB of Ni_2P and their subsequent flow to the

anode back-contact electrode through the appropriately aligned VB of $CuCo_2S_4$, thus resulting to a high catalytic activity for OER.

6. Conclusions

In summary, new nanostructured Ni_2P-modified $CuCo_2S_4$ heterostructures with different content of Ni_2P (15, 20, 30 and 40 wt.%) have been successfully prepared via a two-step hydrothermal method. These materials consist of cubic-phased $CuCo_2S_4$ nanosheets decorated with hexagonal-phased Ni_2P nanoparticles (in 10-15 size) with high crystallinity, according to the X-ray diffraction (XRD), X-ray photoelectron spectroscopy (XPS), high-resolution TEM (HRTEM) and electron diffraction (SAED). The chemical composition of the prepared catalyst was verified by elemental EDS microanalysis. The diffuse reflectance ultraviolet-visible/near-IR (UV-vis/NIR) spectroscopy results revealed that the prepared materials have an optical absorption onset at ~748–757 nm, corresponding to an interband VB-to-CB electron transition of ~1.64 eV for pristine $CuCo_2S_4$ and ~1.65–1.66 eV for $Ni_2P/CuCo_2S_4$ heterostructures. Experimental valence band XPS and electrochemical spectroscopy studies coupled with theoretical DFT calculations indicated that p-n $Ni_2P/CuCo_2S_4$ junctions provide an increased number of electrochemically active surface sites and an efficient interfacial electronic transport with lower resistance, resulting in a remarkable enhancement in the electrocatalytic H_2 evolution performance. Thus, although the unmodified $CuCo_2S_4$ sample showed moderate to low HER performance (348 mV overpotential for 10 $mA \cdot cm^{-2}$), the optimized $Ni_2P/CuCo_2S_4$ catalyst at 30 wt.% Ni_2P content reached an overpotential of 183 mV at 10 $mA \cdot cm^{-2}$ current density under alkaline conditions (1M KOH). The HER activity of 30% $Ni_2P/CuCo_2S_4$ is associated with a 78 $mV \cdot dec^{-1}$ Tafel slope, which is indicative of a Volmer-Heyrovsky type mechanism. Chronopotensiometric studies revealed that this catalyst is quite stable during the course of reaction, operating stably for 30 h under a current density of 10 $mV \cdot cm^{-2}$. In addition, the 30% Ni_2P-loaded catalyst showed a very good oxygen evolution reaction (OER) activity with an overpotential of 360 mV at 40 $mA \cdot cm^{-2}$ current density in 1 M KOH electrolyte. When 30% $Ni_2P/CuCo_2S_4$ is used as both anode and cathode materials in a two-electrode electrochemical cell, it requires only a 1.78 V potential for overall water electrolysis under 10 $mA \cdot cm^{-2}$ current density. Overall, the Ni_2P-modified $CuCo_2S_4$ catalysts demonstrate great potential for the production of renewable and eco-sustainable energy, including water electrolysis and hydrogen evolution.

7. References

(1) Garg, G.; Bobev, S.; Ganguli, A. K. Single Crystal Structure and Electrical Properties of $Cu_8Ni_4Sn_{12}S_{32}$. *J Alloys Compd* **2001**, *327* (1–2), 113–115. https://doi.org/10.1016/S0925-8388(01)01549-3.

(2) Ito, M.; Sonoda, K.; Nagata, S. Temperature Dependence of Thermodynamic Properties of Spinel $CuIr_2S_4$. *Solid State Commun* **2017**, *265*, 23–26. https://doi.org/10.1016/J.SSC.2017.07.021.

(3) Sun, X.; Sun, J.; Wu, C.; Guo, L.; Hou, L.; Yuan, C. Unveiling Composition/Crystal Structure-Dependent Electrochemical Behaviors via Experiments and First-Principles Calculations: Rock-Salt $NiCoO_2$ vs. Spinel $Ni_{1.5}Co_{1.5}O_4$. *Mater Today Energy* **2021**, *19*, 100592. https://doi.org/10.1016/J.MTENER.2020.100592.

(4) Vaughan, D. J.; Craig, J. R. The Crystal Chemistry of Iron-Nickel Thiospinels. *American Mineralogist* **1985**, *70* (9–10).

(5) Ozel, F.; Kılıc, H. S.; Coskun, H.; Deveci, I.; Sarılmaz, A.; Balıkcıoglu, A.; Gundogdu, Y.; Aljabour, A.; Ozen, A.; Gezgin, S. Y.; Houimi, A.; Yar, A.; Kus, M.; Ersoz, M. A General Review on the Thiospinels and Their Energy Applications. *Mater Today Energy* **2021**, *21*, 100822. https://doi.org/10.1016/J.MTENER.2021.100822.

(6) Santos Carballal, D. Computational Studies of Magnetite Fe_3O_4 and Related Spinel-Structured Materials. *Doctoral thesis, UCL (University College London).* **2015**.

(7) Susilo, R. A.; Li, G.; Feng, J.; Deng, W.; Yuan, M.; Li, S.; Dong, H.; Chen, B. Pressure-Induced Structural and Electronic Transitions of Thiospinel Fe_3S_4. *Journal of Physics: Condensed Matter* **2019**, *31* (9), 095401. https://doi.org/10.1088/1361-648X/aafadb.

(8) Park, M. S.; Kwon, S. K.; Min, B. I. Half-Metallic Antiferromagnets in Thiospinels. *Phys Rev B* **2001**, *64* (10), 100403. https://doi.org/10.1103/PhysRevB.64.100403.

(9) Pearce, C. I.; Pattrick, R. A. D.; Vaughan, D. J. Electrical and Magnetic Properties of Sulfides. *Rev Mineral Geochem* **2006**, *61* (1), 127–180. https://doi.org/10.2138/RMG.2006.61.3.

(10) Lee, S. J.; Kim, J. E.; Park, H. Y. Optical Absorption of Co^{2+} in $AgIn_5S_8$ and $CuIn_5S_8$ Spinel Crystals. *Japanese Journal of Applied Physics, Part 1: Regular Papers and Short Notes and Review Papers* **2003**, *42* (6 A), 3337–3339. https://doi.org/10.1143/JJAP.42.3337/XML.

(11) Lee, S.-J.; Kim, J.-E.; Park, H. Y. Optical Absorption of Co^{2+} in $AgIn_5S_8$ and $CuIn_5S_8$ Spinel Crystals. *Jpn J Appl Phys* **2003**, *42* (Part 1, No. 6A), 3337–3339. https://doi.org/10.1143/JJAP.42.3337.

(12) Radautsan, S. I.; Tiginyanu, I. M. Defect Engineering in II-III2-VI4 and Related Compounds. *Jpn J Appl Phys* **1993**, *32* (S3), 5–9. https://doi.org/10.7567/JJAPS.32S3.5/XML.

(13) Hashikuni, K.; Suekuni, K.; Usui, H.; Chetty, R.; Ohta, M.; Kuroki, K.; Takabatake, T.; Watanabe, K.; Ohtaki, M. Thermoelectric Properties and Electronic Structures of $CuTi_2S_4$ Thiospinel and Its Derivatives: Structural Design for Spinel-Related Thermoelectric Materials. *Inorg Chem* **2019**, *58* (2), 1425–1432. https://doi.org/10.1021/ACS.INORGCHEM.8B02955/SUPPL_FILE/IC8B02955_SI_001.PDF

(14) Bourgès, C.; Srinivasan, B.; Fontaine, B.; Sauerschnig, P.; Minard, A.; Halet, J. F.; Miyazaki, Y.; Berthebaud, D.; Mori, T. Tailoring the Thermoelectric and Structural Properties of Cu–Sn

Based Thiospinel Compounds [$CuM_{1+x}Sn_{1-x}S_4$ (M = Ti, V, Cr, Co)]. *J Mater Chem C Mater* **2020**, *8* (46), 16368–16383. https://doi.org/10.1039/D0TC04393A.

(15) Sugita, H.; Wada, S.; Miyatani, K.; Tanaka, T.; Ishikawa, M. An Evidence for the S-Wave Superconductivity of an Itinerant Weak Antiferromagnet $CuCo_2S_4$. *Physica B Condens Matter* **2000**, *284–288* (PART I), 473–474. https://doi.org/10.1016/S0921-4526(99)02040-2.

(16) Wada, S.; Sugita, H.; Miyatani, K.; Tanaka, T.; Nishikawa, T. Weak Antiferromagnetism and Superconductivity in Pseudo-Binary Compounds (Cu,Co)Co_2S_4 Investigated by 59Co and 63Cu Magnetic Resonance. *Journal of Physics: Condensed Matter* **2001**, *14* (2), 219. https://doi.org/10.1088/0953-8984/14/2/309.

(17) Lee, S. J.; Kim, J. E.; Park, H. Y. Optical Absorption of Co^{2+} in $MgIn_2S_4$, $CdIn_2S_4$, and $HgIn_2S_4$ Spinel Crystals. *Journal of Materials Research 2003 18:3* **2003**, *18* (3), 733–736. https://doi.org/10.1557/JMR.2003.0099.

(18) Gundogdu, Y.; Sarilmaz, A.; Gencer, A.; Ozel, F.; Surucu, G.; Kilic, H. S.; Ersoz, M. Copper-Based Thiospinel Quantum Dots as Potential Candidates for Nonlinear Optical Applications. *Opt Laser Technol* **2022**, *148*, 107752. https://doi.org/10.1016/J.OPTLASTEC.2021.107752.

(19) Kale, B. B.; Baeg, J. O.; Lee, S. M.; Chang, H.; Moon, S. J.; Lee, C. W. $CdIn_2S_4$ Nanotubes and "Marigold" Nanostructures: A Visible-Light Photocatalyst. *Adv Funct Mater* **2006**, *16* (10), 1349–1354. https://doi.org/10.1002/ADFM.200500525.

(20) Bhirud, A.; Chaudhari, N.; Nikam, L.; Sonawane, R.; Patil, K.; Baeg, J. O.; Kale, B. Surfactant Tunable Hierarchical Nanostructures of $CdIn_2S_4$ and Their Photohydrogen Production under Solar Light. *Int J Hydrogen Energy* **2011**, *36* (18), 11628–11639. https://doi.org/10.1016/J.IJHYDENE.2011.06.061.

(21) Peng, S.; Mhaisalkar, S. G.; Ramakrishna, S. Solution Synthesis of $CdIn_2S_4$ Nanocrystals and Their Photoelectrical Application. *Mater Lett* **2012**, *79*, 216–218. https://doi.org/10.1016/J.MATLET.2012.04.014.

(22) Zhou, Q.; Zheng, Z.; Zhang, Y.; Kang, S.; Li, X.; Mu, J. Synthesis of $CdIn_2S_4$ Nanosheets in a Mercaptoacetic Acid-Assisted Hydrothermal Process. *Mater Lett* **2014**, *124*, 61–63. https://doi.org/10.1016/J.MATLET.2014.03.063.

(23) Song, Y.; Chen, Z.; Li, Y.; Wang, Q.; Fang, F.; Zhou, Y. N.; Hu, L.; Sun, D. Pseudocapacitance-Tuned High-Rate and Long-Term Cyclability of $NiCo_2S_4$ Hexagonal Nanosheets Prepared by Vapor Transformation for Lithium Storage. *J Mater Chem A Mater* **2017**, *5* (19), 9022–9031. https://doi.org/10.1039/c7ta01758h.

(24) Song, Y.; Li, Y.; Zhu, L.; Pan, Z.; Jiang, Y.; Wang, P.; Zhou, Y. N.; Fang, F.; Hu, L.; Sun, D. $CuGaS_2$ Nanoplates: A Robust and Self-Healing Anode for Li/Na Ion Batteries in a Wide Temperature Range of 268-318 K. *J Mater Chem A Mater* **2018**, *6* (3), 1086–1093. https://doi.org/10.1039/c7ta09197d.

(25) Saravanakumar, T.; Selvaraju, T.; Bhojanaa, K. B.; Ramesh, M.; Pandikumar, A.; Akilan, R.; Shankar, R.; Sardhar Basha, S. J. Exploring the Synergistic Effect of $Ni:_XSn_{2X}S_{4x}$ Thiospinel with MWCNTs for Enhanced Performance in Dye-Sensitized Solar Cells, the Hydrogen Evolution Reaction, and Supercapacitors. *Dalton Transactions* **2020**, *49* (16), 5336–5351. https://doi.org/10.1039/d0dt00839g.

(26) Wang, X. W.; Li, X. Z.; Wu, K. L.; Zhao, M. L.; Yue, Y. X.; Cheng, J.; Ma, C. C.; Ming, J.; Wei, X. W. Shape-Controlled Synthesis of $CoNi_2S_4$ Microstructures from Precursors: A Study

of Their Catalytic Application to p-Nitrophenol Reduction. *https://doi.org/10.1246/cl.140504* **2014**, *43* (10), 1590–1592. https://doi.org/10.1246/CL.140504.

(27) Guo, K.; Ding, Y.; Luo, J.; Yu, Z. Nickel Cobalt Thiospinel Nanoparticles as Hydrodesulfurization Catalysts: Importance of Cation Position, Structural Stability, and Sulfur Vacancy. *ACS Appl Mater Interfaces* **2018**, *10* (23), 19673–19681. https://doi.org/10.1021/ACSAMI.8B03588/SUPPL_FILE/AM8B03588_SI_001.PDF.

(28) Mitchell, C. E.; Santos-Carballal, D.; Beale, A. M.; Jones, W.; Morgan, D. J.; Sankar, M.; de Leeuw, N. H. The Role of Surface Oxidation and Fe–Ni Synergy in Fe–Ni–S Catalysts for CO2 Hydrogenation. *Faraday Discuss* **2021**, *230* (0), 30–51. https://doi.org/10.1039/D0FD00137F.

(29) Soni, K.; Chauhan, M.; Deka, S. Hydrothermally Synthesized $CuCo_2S_4$ Nanosheets as an Easily Accessible and Convenient Heterogeneous Catalyst for the Sonogashira Cross-Coupling Reactions. *Front Mater* **2019**, *6*, 273. https://doi.org/10.3389/FMATS.2019.00273/BIBTEX.

(30) Crabtree, G. W.; Dresselhaus, M. S.; Buchanan, M. v. The Hydrogen Economy. *Phys Today* **2007**, *57* (12), 39. https://doi.org/10.1063/1.1878333.

(31) Züttel, A.; Remhof, A.; Borgschulte, A.; Friedrichs, O. Hydrogen: The Future Energy Carrier. *Philosophical Transactions of the Royal Society A: Mathematical, Physical and Engineering Sciences* **2010**, *368* (1923), 3329–3342. https://doi.org/10.1098/RSTA.2010.0113.

(32) Fu, G.; Lee, J. M. Ternary Metal Sulfides for Electrocatalytic Energy Conversion. *J Mater Chem A Mater* **2019**, *7* (16), 9386–9405. https://doi.org/10.1039/C9TA01438A.

(33) Singh, N.; Gordon, M.; Metiu, H.; McFarland, E. Doped Rhodium Sulfide and Thiospinels Hydrogen Evolution and Oxidation Electrocatalysts in Strong Acid Electrolytes. *Journal of Applied Electrochemistry 2016 46:4* **2016**, *46* (4), 497–503. https://doi.org/10.1007/S10800-016-0938-0.

(34) Gervas, C.; Khan, M. D.; Zhang, C.; Zhao, C.; Gupta, R. K.; Carleschi, E.; Doyle, B. P.; Revaprasadu, N. Effect of Cationic Disorder on the Energy Generation and Energy Storage Applications of $Ni_xCo_{3-x}S_4$ Thiospinel. *RSC Adv* **2018**, *8* (42), 24049–24058. https://doi.org/10.1039/C8RA03522A.

(35) Liu, D.; Lu, Q.; Luo, Y.; Sun, X.; Asiri, A. M. NiCo2S4 Nanowires Array as an Efficient Bifunctional Electrocatalyst for Full Water Splitting with Superior Activity. *Nanoscale* **2015**, *7* (37), 15122–15126. https://doi.org/10.1039/C5NR04064G.

(36) Sivanantham, A.; Ganesan, P.; Shanmugam, S. Hierarchical $NiCo_2S_4$ Nanowire Arrays Supported on Ni Foam: An Efficient and Durable Bifunctional Electrocatalyst for Oxygen and Hydrogen Evolution Reactions. *Adv Funct Mater* **2016**, *26* (26), 4661–4672. https://doi.org/10.1002/ADFM.201600566.

(37) Wu, X.; Li, S.; Liu, J.; Yu, M. Mesoporous Hollow Nested Nanospheres of Ni, Cu, Co-Based Mixed Sulfides for Electrocatalytic Oxygen Reduction and Evolution. *ACS Appl Nano Mater* **2019**, *2* (8), 4921–4932. https://doi.org/10.1021/ACSANM.9B00891/SUPPL_FILE/AN9B00891_SI_001.PDF.

(38) Wan, K.; Luo, J.; Zhou, C.; Zhang, T.; Arbiol, J.; Lu, X.; Mao, B. W.; Zhang, X.; Fransaer, J. Hierarchical Porous Ni_3S_4 with Enriched High-Valence Ni Sites as a Robust Electrocatalyst for Efficient Oxygen Evolution Reaction. *Adv Funct Mater* **2019**, *29* (18), 1900315. https://doi.org/10.1002/ADFM.201900315.

(39) Wiltrout, A. M.; Read, C. G.; Spencer, E. M.; Schaak, R. E. Solution Synthesis of Thiospinel $CuCo_2S_4$ Nanoparticles. *Inorg. Chem* **2016**, *55*, 24. https://doi.org/10.1021/acs.inorgchem.5b02158.

(40) Chauhan, M.; Reddy, K. P.; Gopinath, C. S.; Deka, S. Copper Cobalt Sulfide Nanosheets Realizing a Promising Electrocatalytic Oxygen Evolution Reaction. *ACS Catal* **2017**, *7* (9), 5871–5879. https://doi.org/10.1021/ACSCATAL.7B01831/ASSET/IMAGES/LARGE/CS-2017-01831K_0006.JPEG.

(41) Tang, S.; Wang, X.; Zhang, Y.; Courté, M.; Fan, H. J.; Fichou, D. Combining Co_3S_4 and Ni:Co_3S_4 Nanowires as Efficient Catalysts for Overall Water Splitting: An Experimental and Theoretical Study. *Nanoscale* **2019**, *11* (5), 2202–2210. https://doi.org/10.1039/C8NR07787H.

(42) Wang, D.; Zhang, X.; Du, Z.; Mo, Z.; Wu, Y.; Yang, Q.; Zhang, Y.; Wu, Z. $CoNi_2S_4$ Nanoparticles as Highly Efficient Electrocatalysts for the Hydrogen Evolution Reaction in Alkaline Media. *Int J Hydrogen Energy* **2017**, *42* (5), 3043–3050. https://doi.org/10.1016/J.IJHYDENE.2016.09.115.

(43) Huang, D. D.; Li, S.; Wu, Y. P.; Wei, J. H.; Yi, J. W.; Ma, H. M.; Zhang, Q. C.; Liu, Y. L.; Li, D. S. In Situ Synthesis of a Fe_3S_4/MIL-53(Fe) Hybrid Catalyst for an Efficient Electrocatalytic Hydrogen Evolution Reaction. *Chemical Communications* **2019**, *55* (31), 4570–4573. https://doi.org/10.1039/C9CC01433K.

(44) Ge, Y.; Wu, J.; Xu, X.; Ye, M.; Shen, J. Facile Synthesis of $CoNi_2S_4$ and $CuCo_2S_4$ with Different Morphologies as Prominent Catalysts for Hydrogen Evolution Reaction. *Int J Hydrogen Energy* **2016**, *41* (44), 19847–19854. https://doi.org/10.1016/J.IJHYDENE.2016.08.096.

(45) Hao, Z.; Wei, P.; Kang, H.; Yang, Y.; Li, J.; Chen, X.; Guo, D.; Liu, L. Three-Dimensional Fe_3S_4@NiS Hollow Nanospheres as Efficient Electrocatalysts for Oxygen Evolution Reaction. *Journal of Electroanalytical Chemistry* **2019**, *850*, 113436. https://doi.org/10.1016/J.JELECHEM.2019.113436.

(46) Zhao, S.; Wang, Y.; Zhang, Q.; Li, Y.; Gu, L.; Dai, Z.; Liu, S.; Lan, Y. Q.; Han, M.; Bao, J. Two-Dimensional Nanostructures of Non-Layered Ternary Thiospinels and Their Bifunctional Electrocatalytic Properties for Oxygen Reduction and Evolution: The Case of $CuCo_2S_4$ Nanosheets. *Inorg Chem Front* **2016**, *3* (12), 1501–1509. https://doi.org/10.1039/C6QI00355A.

(47) Xu, H.; Wang, D.; Ma, J.; Zhang, T.; Lu, X.; Chen, Z. A Superior Active and Stable Spinel Sulfide for Catalytic Peroxymonosulfate Oxidation of Bisphenol S. *Appl Catal B* **2018**, *238*, 557–567. https://doi.org/10.1016/J.APCATB.2018.07.058.

(48) Buckley, A. N.; Skinner, W. M.; Harmer, S. L.; Pring, A.; Fan, L. J. Electronic Environments in Carrollite, $CuCo_2S_4$, Determined by Soft X-Ray Photoelectron and Absorption Spectroscopy. *Geochim Cosmochim Acta* **2009**, *73* (15), 4452–4467. https://doi.org/10.1016/J.GCA.2009.05.030.

(49) Huang, X.; Deng, G.; Liao, L.; Zhang, W.; Guan, G.; Zhou, F.; Xiao, Z.; Zou, R.; Wang, Q.; Hu, J. $CuCo_2S_4$ Nanocrystals: A New Platform for Multimodal Imaging Guided Photothermal Therapy. *Nanoscale* **2017**, *9* (7), 2626–2632. https://doi.org/10.1039/C6NR09028A.

(50) Li, B.; Yuan, F.; He, G.; Han, X.; Wang, X.; Qin, J.; Guo, Z. X.; Lu, X.; Wang, Q.; Parkin, I. P.; Wu, C. Ultrasmall $CuCo_2S_4$ Nanocrystals: All-in-One Theragnosis Nanoplatform with

Magnetic Resonance/Near-Infrared Imaging for Efficiently Photothermal Therapy of Tumors. *Adv Funct Mater* **2017**, *27* (10), 1606218. https://doi.org/10.1002/ADFM.201606218.

(51) Chen, Y.; Ji, X.; Sethumathavan, V.; Paul, B. Facile Solvothermal Synthesis of $CuCo_2S_4$ Yolk-Shells and Their Visible-Light-Driven Photocatalytic Properties. *Materials 2018, Vol. 11, Page 2303* **2018**, *11* (11), 2303. https://doi.org/10.3390/MA11112303.

(52) Vadivel, S.; Paul, B.; Habibi-Yangjeh, A.; Maruthamani, D.; Kumaravel, M.; Maiyalagan, T. One-Pot Hydrothermal Synthesis of $CuCo_2S_4$/RGO Nanocomposites for Visible-Light Photocatalytic Applications. *Journal of Physics and Chemistry of Solids* **2018**, *123*, 242–253. https://doi.org/10.1016/J.JPCS.2018.08.011.

(53) Sarilmaz, A.; Yanalak, G.; Aslan, E.; Akyildiz, H.; Patir, I. H.; Ozel, F. Ternary and Quaternary Thiospinel Nanocrystals with Adjustable Compositions: Effects of Band-Gaps and Nanostructures on Visible-Light-Driven Photocatalytic H2 Evolution. *Mater Today Energy* **2020**, *16*, 100413. https://doi.org/10.1016/J.MTENER.2020.100413.

(54) Chauhan, M.; Soni, K.; Karthik, P. E.; Reddy, K. P.; Gopinath, C. S.; Deka, S. Promising Visible-Light Driven Hydrogen Production from Water on a Highly Efficient $CuCo_2S_4$ Nanosheet Photocatalyst. *J Mater Chem A Mater* **2019**, *7* (12), 6985–6994. https://doi.org/10.1039/C9TA00391F.

(55) Lang, Y.; Pan, L.; Chen, C.; Wang, Y. Thermoelectric Properties of Thiospinel-Type $CuCo_2S_4$. *Journal of Electronic Materials 2019 48:7* **2019**, *48* (7), 4179–4187. https://doi.org/10.1007/S11664-019-07182-X.

(56) Tang, J.; Ge, Y.; Shen, J.; Ye, M. Facile Synthesis of CuCo2S4 as a Novel Electrode Material for Ultrahigh Supercapacitor Performance. *Chemical Communications* **2016**, *52* (7), 1509–1512. https://doi.org/10.1039/C5CC09402J.

(57) Zhu, Y.; Ji, X.; Chen, H.; Xi, L.; Gong, W.; Liu, Y. The Investigation of the Electrochemically Supercapacitive Performances of Mesoporous $CuCo_2S_4$. *RSC Adv* **2016**, *6* (87), 84236–84241. https://doi.org/10.1039/C6RA20120B.

(58) Czioska, S.; Wang, J.; Teng, X.; Chen, Z. Hierarchically Structured $CuCo_2S_4$ Nanowire Arrays as Efficient Bifunctional Electrocatalyst for Overall Water Splitting. *ACS Sustain Chem Eng* **2018**, *6* (9), 11877–11883. https://doi.org/10.1021/ACSSUSCHEMENG.8B02155/SUPPL_FILE/SC8B02155_SI_001.PDF.

(59) Shao, L.; Liang, Z. X.; Chen, H.; Song, Z. X.; Deng, X. H.; Huo, G.; Kang, X. M.; Wang, L.; Fu, X. Z.; Luo, J. L. $CuCo_2S_4$ Hollow Nanoneedle Arrays Supported on Ni Foam as Efficient Trifunctional Electrocatalysts for Overall Water Splitting and Al–Air Batteries. *J Alloys Compd* **2020**, *845*, 155392. https://doi.org/10.1016/J.JALLCOM.2020.155392.

(60) Ren, C.; Chen, Y.; Du, L.; Wang, Q.; Li, L.; Tian, G. Hierarchical $CuCo_2S_4$ Nanoflake Arrays Grown on Carbon Cloth: A Remarkable Bifunctional Electrocatalyst for Overall Water Splitting. *ChemElectroChem* **2021**, *8* (6), 1134–1140. https://doi.org/10.1002/CELC.202100247.

(61) Carenco, S.; Portehault, D.; Boissière, C.; Mézailles, N.; Sanchez, C. Nanoscaled Metal Borides and Phosphides: Recent Developments and Perspectives. *Chem Rev* **2013**, *113* (10), 7981–8065. https://doi.org/10.1021/CR400020D/ASSET/IMAGES/CR400020D.SOCIAL.JPEG_V03.

(62) Du, H.; Kong, R. M.; Guo, X.; Qu, F.; Li, J. Recent Progress in Transition Metal Phosphides with Enhanced Electrocatalysis for Hydrogen Evolution. *Nanoscale* **2018**, *10* (46), 21617–21624. https://doi.org/10.1039/C8NR07891B.

(63) Sun, M.; Liu, H.; Qu, J.; Li, J. Earth-Rich Transition Metal Phosphide for Energy Conversion and Storage. *Adv Energy Mater* **2016**, *6* (13). https://doi.org/10.1002/AENM.201600087.

(64) Laursen, A. B.; Patraju, K. R.; Whitaker, M. J.; Retuerto, M.; Sarkar, T.; Yao, N.; Ramanujachary, K. v.; Greenblatt, M.; Dismukes, G. C. Nanocrystalline Ni_5P_4: A Hydrogen Evolution Electrocatalyst of Exceptional Efficiency in Both Alkaline and Acidic Media. *Energy Environ Sci* **2015**, *8* (3), 1027–1034. https://doi.org/10.1039/C4EE02940B.

(65) Lin, Y.; Pan, Y.; Zhang, J. In Situ Construction of Nickel Phosphosulfide (Ni_5P_4|S) Active Species on 3D Ni Foam through Chemical Vapor Deposition for Electrochemical Hydrogen Evolution. *ChemElectroChem* **2017**, *4* (5), 1108–1116. https://doi.org/10.1002/CELC.201600808.

(66) Moon, J. S.; Jang, J. H.; Kim, E. G.; Chung, Y. H.; Yoo, S. J.; Lee, Y. K. The Nature of Active Sites of Ni_2P Electrocatalyst for Hydrogen Evolution Reaction. *J Catal* **2015**, *326*, 92–99. https://doi.org/10.1016/J.JCAT.2015.03.012.

(67) Popczun, E. J.; McKone, J. R.; Read, C. G.; Biacchi, A. J.; Wiltrout, A. M.; Lewis, N. S.; Schaak, R. E. Nanostructured Nickel Phosphide as an Electrocatalyst for the Hydrogen Evolution Reaction. *J Am Chem Soc* **2013**, *135* (25), 9267–9270. https://doi.org/10.1021/JA403440E/SUPPL_FILE/JA403440E_SI_001.PDF.

(68) Ray, A.; Sultana, S.; Paramanik, L.; Parida, K. M. Recent Advances in Phase, Size, and Morphology-Oriented Nanostructured Nickel Phosphide for Overall Water Splitting. *J Mater Chem A Mater* **2020**, *8* (37), 19196–19245. https://doi.org/10.1039/D0TA05797E.

(69) Lyu, F.; Wang, Q.; Choi, S. M.; Yin, Y. Noble-Metal-Free Electrocatalysts for Oxygen Evolution. *Small* **2019**, *15* (1), 1804201. https://doi.org/10.1002/SMLL.201804201.

(70) Li, Y.; Zhou, L.; Guo, S. Noble Metal-Free Electrocatalytic Materials for Water Splitting in Alkaline Electrolyte. *EnergyChem* **2021**, *3* (2), 100053. https://doi.org/10.1016/J.ENCHEM.2021.100053.

(71) Roger, I.; Shipman, M. A.; Symes, M. D. Earth-Abundant Catalysts for Electrochemical and Photoelectrochemical Water Splitting. *Nature Reviews Chemistry 2017 1:1* **2017**, *1* (1), 1–13. https://doi.org/10.1038/s41570-016-0003.

(72) Shi, Q.; Zhu, C.; Du, D.; Lin, Y. Robust Noble Metal-Based Electrocatalysts for Oxygen Evolution Reaction. *Chem Soc Rev* **2019**, *48* (12), 3181–3192. https://doi.org/10.1039/C8CS00671G.

(73) Xiong, B.; Chen, L.; Shi, J. Anion-Containing Noble-Metal-Free Bifunctional Electrocatalysts for Overall Water Splitting. *ACS Catal* **2018**, *8* (4), 3688–3707. https://doi.org/10.1021/ACSCATAL.7B04286/ASSET/IMAGES/MEDIUM/CS-2017-04286E_0010.GIF.

(74) Wang, J.; Cui, W.; Liu, Q.; Xing, Z.; Asiri, A. M.; Sun, X. Recent Progress in Cobalt-Based Heterogeneous Catalysts for Electrochemical Water Splitting. *Advanced Materials* **2016**, *28* (2), 215–230. https://doi.org/10.1002/ADMA.201502696.

(75) Cai, Z.; Bu, X.; Wang, P.; Ho, J. C.; Yang, J.; Wang, X. Recent Advances in Layered Double Hydroxide Electrocatalysts for the Oxygen Evolution Reaction. *J Mater Chem A Mater* **2019**, *7* (10), 5069–5089. https://doi.org/10.1039/C8TA11273H.

(76) Xie, L.; Zhang, R.; Cui, L.; Liu, D.; Hao, S.; Ma, Y.; Du, G.; Asiri, A. M.; Sun, X. High-Performance Electrolytic Oxygen Evolution in Neutral Media Catalyzed by a Cobalt Phosphate Nanoarray. *Angewandte Chemie International Edition* **2017**, *56* (4), 1064–1068. https://doi.org/10.1002/ANIE.201610776.

(77) Zhang, H.; Guan, D.; Gao, X.; Yu, J.; Chen, G.; Zhou, W.; Shao, Z. Morphology, Crystal Structure and Electronic State One-Step Co-Tuning Strategy towards Developing Superior Perovskite Electrocatalysts for Water Oxidation. *J Mater Chem A Mater* **2019**, *7* (33), 19228–19233. https://doi.org/10.1039/C9TA06020K.

(78) Yu, J.; Guo, Y.; She, S.; Miao, S.; Ni, M.; Zhou, W.; Liu, M.; Shao, Z. Bigger Is Surprisingly Better: Agglomerates of Larger RuP Nanoparticles Outperform Benchmark Pt Nanocatalysts for the Hydrogen Evolution Reaction. *Advanced Materials* **2018**, *30* (39), 1800047. https://doi.org/10.1002/ADMA.201800047.

(79) Yu, J.; Zhong, Y.; Wu, X.; Sunarso, J.; Ni, M.; Zhou, W.; Shao, Z. Bifunctionality from Synergy: CoP Nanoparticles Embedded in Amorphous CoOx Nanoplates with Heterostructures for Highly Efficient Water Electrolysis. *Advanced Science* **2018**, *5* (9). https://doi.org/10.1002/ADVS.201800514.

(80) Kim, J. S.; Kim, B.; Kim, H.; Kang, K. Recent Progress on Multimetal Oxide Catalysts for the Oxygen Evolution Reaction. *Adv Energy Mater* **2018**, *8* (11), 1–26. https://doi.org/10.1002/aenm.201702774.

(81) Lyu, F.; Wang, Q.; Choi, S. M.; Yin, Y. Noble-Metal-Free Electrocatalysts for Oxygen Evolution. *Small* **2019**, *15* (1), 1–17. https://doi.org/10.1002/smll.201804201.

(82) Yu, J.; Dai, Y.; He, Q.; Cheng, C.; Shao, Z.; Ni, M. Robust Non-Pt Noble Metal-Based Nanomaterials for Electrocatalytic Hydrogen Generation. *Appl Phys Rev* **2020**, *7* (4). https://doi.org/10.1063/5.0021578.

(83) Shi, Y.; Zhang, B. Recent Advances in Transition Metal Phosphide Nanomaterials: Synthesis and Applications in Hydrogen Evolution Reaction. *Chem Soc Rev* **2016**, *45* (6), 1529–1541. https://doi.org/10.1039/c5cs00434a.

(84) Xiao, P.; Sk, M. A.; Thia, L.; Ge, X.; Lim, R. J.; Wang, J. Y.; Lim, K. H.; Wang, X. Molybdenum Phosphide as an Efficient Electrocatalyst for the Hydrogen Evolution Reaction. *Energy Environ Sci* **2014**, *7* (8), 2624–2629. https://doi.org/10.1039/c4ee00957f.

(85) Wu, R.; Zhang, J.; Shi, Y.; Liu, D.; Zhang, B. Metallic WO_2-Carbon Mesoporous Nanowires as Highly Efficient Electrocatalysts for Hydrogen Evolution Reaction. *J Am Chem Soc* **2015**, *137* (22), 6983–6986. https://doi.org/10.1021/jacs.5b01330.

(86) Patra, B. C.; Khilari, S.; Manna, R. N.; Mondal, S.; Pradhan, D.; Pradhan, A.; Bhaumik, A. A Metal-Free Covalent Organic Polymer for Electrocatalytic Hydrogen Evolution. *ACS Catal* **2017**, *7* (9), 6120–6127. https://doi.org/10.1021/acscatal.7b01067.

(87) Chauhan, M.; Soni, K.; Karthik, P. E.; Reddy, K. P.; Gopinath, C. S.; Deka, S. Promising Visible-Light Driven Hydrogen Production from Water on a Highly Efficient $CuCo_2S_4$ Nanosheet Photocatalyst. *J Mater Chem A Mater* **2019**, *7* (12), 6985–6994. https://doi.org/10.1039/c9ta00391f.

(88) Kaplan, H. K.; Akay, S. K.; Ahmetoğlu, M. A Novel Self-Powered Filterless Narrow-Band near-Infrared Photodiode of Cu_2S/Si P+-p Isotype Heterojunction Device with Very Low Visible Light Noise. *Appl Surf Sci* **2022**, *601*, 154217. https://doi.org/10.1016/J.APSUSC.2022.154217.

(89) Krylova, V.; Andruleviçius, M. Optical, XPS and XRD Studies of Semiconducting Copper Sulfide Layers on a Polyamide Film. *International Journal of Photoenergy* **2009**, *2009*. https://doi.org/10.1155/2009/304308.

(90) Chen, B.; Li, X.; Rui, P.; Ye, Y.; Ye, T.; Zhou, R.; Li, D.; Carter, J. H.; Hutchings, G. J. The Reaction Pathways of 5-Hydroxymethylfurfural Conversion in a Continuous Flow Reactor Using Copper Catalysts. *Catal Sci Technol* **2022**, *12* (9), 3016–3027. https://doi.org/10.1039/D1CY02197D.

(91) Czioska, S.; Wang, J.; Teng, X.; Chen, Z. Hierarchically Structured $CuCo_2S_4$ Nanowire Arrays as Efficient Bifunctional Electrocatalyst for Overall Water Splitting. *ACS Sustain Chem Eng* **2018**, *6* (9), 11877–11883. https://doi.org/10.1021/ACSSUSCHEMENG.8B02155/SUPPL_FILE/SC8B02155_SI_001.PDF.

(92) Shao, L.; Liang, Z. X.; Chen, H.; Song, Z. X.; Deng, X. H.; Huo, G.; Kang, X. M.; Wang, L.; Fu, X. Z.; Luo, J. L. $CuCo_2S_4$ Hollow Nanoneedle Arrays Supported on Ni Foam as Efficient Trifunctional Electrocatalysts for Overall Water Splitting and Al–Air Batteries. *J Alloys Compd* **2020**, *845*, 155392. https://doi.org/10.1016/J.JALLCOM.2020.155392.

(93) Ren, C.; Chen, Y.; Du, L.; Wang, Q.; Li, L.; Tian, G. Hierarchical $CuCo_2S_4$ Nanoflake Arrays Grown on Carbon Cloth: A Remarkable Bifunctional Electrocatalyst for Overall Water Splitting. *ChemElectroChem* **2021**, *8* (6), 1134–1140. https://doi.org/10.1002/CELC.202100247.

(94) Zhang, R.; Hu, Z.; Cheng, S.; Ke, W.; Ning, T.; Wu, J.; Fu, X.; Zhu, G. Molecular Precursor Route to $CuCo_2S_4$ Nanosheets: A High-Performance Pre-Catalyst for Oxygen Evolution and Its Application in Zn-Air Batteries. *Inorg Chem* **2021**, *60* (9), 6721–6730. https://doi.org/10.1021/ACS.INORGCHEM.1C00545/SUPPL_FILE/IC1C00545_SI_001.PDF.

(95) Wang, W.; An, T.; Li, G.; Xia, D.; Zhao, H.; Yu, J. C.; Wong, P. K. Earth-Abundant Ni_2P/g-C_3N_4 Lamellar Nanohydrids for Enhanced Photocatalytic Hydrogen Evolution and Bacterial Inactivation under Visible Light Irradiation. *Appl Catal B* **2017**, *217*, 570–580. https://doi.org/10.1016/J.APCATB.2017.06.027.

(96) Zhen, W.; Ning, X.; Yang, B.; Wu, Y.; Li, Z.; Lu, G. The Enhancement of CdS Photocatalytic Activity for Water Splitting via Anti-Photocorrosion by Coating Ni_2P Shell and Removing Nascent Formed Oxygen with Artificial Gill. *Appl Catal B* **2018**, *221*, 243–257. https://doi.org/10.1016/J.APCATB.2017.09.024.

(97) You, B.; Zhang, Y.; Jiao, Y.; Davey, K.; Qiao, S. Z. Negative Charging of Transition-Metal Phosphides via Strong Electronic Coupling for Destabilization of Alkaline Water. *Angewandte Chemie International Edition* **2019**, *58* (34), 11796–11800. https://doi.org/10.1002/ANIE.201906683.

(98) You, B.; Liu, X.; Hu, G.; Gul, S.; Yano, J.; Jiang, D. E.; Sun, Y. Universal Surface Engineering of Transition Metals for Superior Electrocatalytic Hydrogen Evolution in Neutral Water. *J Am Chem Soc* **2017**, *139* (35), 12283–12290. https://doi.org/10.1021/JACS.7B06434/SUPPL_FILE/JA7B06434_SI_001.PDF.

(99) Zhang, Y.; Xiao, X.; Wang, X.; Jiang, X.; Gao, X.; Li, P.; Shen, Y. Boosting Electrocatalytic Activity of Ni_2P Nanosheets via Incorporation of Ru Nanoparticles for Efficient Hydrogen Generation in Alkaline Media. *Appl Surf Sci* **2021**, *554*, 149560. https://doi.org/10.1016/J.APSUSC.2021.149560.

(100) Zhao, H.; Liang, J.; Zhao, Y. Construction of Hierarchical Co_2P/Ni_2P Heterostructures on Ni Foam as Efficient Bifunctional Electrocatalyst for Overall Water Splitting. *J Alloys Compd* **2022**, *907*, 164479. https://doi.org/10.1016/J.JALLCOM.2022.164479.

(101) Trasatti, S.; Petrii, O. A. Real Surface Area Measurements in Electrochemistry. *Journal of Electroanalytical Chemistry* **1992**, *327* (1–2), 353–376. https://doi.org/10.1016/0022-0728(92)80162-W.

(102) *Allen J. Bard and Larry R. Faulkner, Electrochemical Methods: Fundamentals and Applications, New York: Wiley, 2001, 2nd Ed.*; Springer, 2002. https://doi.org/10.1023/A:1021637209564.

(103) McCrory, C. C. L.; Jung, S.; Peters, J. C.; Jaramillo, T. F. Benchmarking Heterogeneous Electrocatalysts for the Oxygen Evolution Reaction. *J Am Chem Soc* **2013**, *135* (45), 16977–16987. https://doi.org/10.1021/JA407115P/SUPPL_FILE/JA407115P_SI_001.PDF.